Acta Pharmaceutica Sinica B 2026;16(7):4389−4409

Chinese Pharmaceutical Association
Institute of Materia Medica, Chinese Academy of Medical Sciences

Acta Pharmaceutica Sinica B

www.elsevier.com/locate/apsb
www.sciencedirect.com

ORIGINAL ARTICLE

Attenuating AAV-triggered innate immunity in the adult mouse nervous system *via* cGAS−STING pathway inhibition

Yaowei Guo, Jiehao Huang, Yuqi Zhang, Yuxiang Huang, Zeru Li, Yu Xie, Yingqi Cao, Kun Qian, Fan Bai, Wen Li, Wenliang Lei*, Gong Chen*, Zheng Wu*

State Key Laboratory of Bioactive Molecules and Druggability Assessment, Guangdong Basic Research Center of Excellence for Natural Bioactive Molecules and Discovery of Innovative Drugs, Key Laboratory of CNS Regeneration (Ministry of Education), Guangdong Key Laboratory of Non-Human Primate Research, GHM Institute of CNS Regeneration, Jinan University, Guangzhou 510632, China

Received 31 August 2025; received in revised form 17 November 2025; accepted 4 January 2026

KEY WORDS

AAV;
Innate immunity;
Gene therapy;
cGAS−STING;
Nervous system;
Neuroinflammation;
Microglia

Abstract While adeno-associated virus (AAV)-mediated gene delivery has emerged as a promising therapeutic modality for neurological disorders, dose-dependent immune responses remain a critical barrier to clinical translation. Here we reveal the cyclic GMP−AMP synthase-stimulator of interferon genes (cGAS−STING) pathway as a key mediator of innate immune activation following intracranial AAV administration. Through comparative analyses in genetic and pharmacological intervention models, we demonstrate that STING signaling mediates key neuroinflammatory sequelae including glia reactivation, cytotoxic T cell infiltration, and neuronal injury. Mechanistically, microglia serve as the predominant sentinels detecting AAV immunogenicity *via* cGAS−STING activation. Therapeutic inhibition of this pathway by either microglia depletion or antagonism of STING by small molecules significantly mitigates high-dose AAV9-induced neurotoxicity while enhancing transgene delivery efficacy. Our work delineates a unified mechanistic framework linking AAV-triggered DNA sensing to neuroinflammatory pathology, and provides two clinically actionable approaches to decouple therapeutic gene delivery from detrimental immune activation in nervous system targeted gene therapy.

*Corresponding authors.
E-mail addresses: leiwenliang@jnu.edu.cn (Wenliang Lei), gongchen@jnu.edu.cn (Gong Chen), zhengwu@jnu.edu.cn (Zheng Wu).

Peer review under the responsibility of Chinese Pharmaceutical Association and Institute of Materia Medica, Chinese Academy of Medical Sciences.

https://doi.org/10.1016/j.apsb.2026.04.001

1. Introduction

Adeno-associated virus (AAV) has emerged as an optimal vector for clinical gene delivery, attributable to its minimal pathogenicity and capacity for sustained expression of therapeutic genes across diverse cell types[1-3]. Empirical evidence garnered from clinical trials suggests a significant positive correlation between the administered dose of AAV and the resultant treatment efficacy[4-6]. However, a critical challenge associated with AAV gene therapies is the potential for eliciting immune responses and inflammation, which can compromise the efficacy and durability of the therapeutic intervention, and in rare cases, be life-threatening[7−9]. Therefore, optimization of adeno-associated virus (AAV) gene therapy requires a delicate balance between dose and efficacy, as adequate vector doses are required to elicit a therapeutic response, whereas excessive doses may produce undesirable toxic effects. Consequently, continued advancement of AAV-based therapies requires ongoing research efforts focused on optimizing treatment regimens and vector design, with the ultimate goal of providing patients with safer and more effective treatment options.

The central nervous system (CNS) has traditionally been considered an immune-privileged site, and thus CNS immune responses to AAV gene therapy are often overlooked[10,11]. To ensure adequate expression of therapeutic genes in the CNS, large doses of AAV therapeutic vectors are often injected[1,12]. However, studies in rodents and nonhuman primates (NHPs) have shown that both local and systemic treatments with AAV vectors can induce dose-dependent toxicity in the CNS, characterized by activated immune response, reactive glia and neuronal dysfunction[13-16]. AAV consists of a single-stranded DNA (ssDNA) genome of approximately 4.7 kb enclosed by a capsid of approximately 26 nm in diameter, and both the AAV capsid and genome serve as immunogenic components[17-19]. Our previous study indicated that intraparenchymal injection of high-titer AAV vectors induced a significant immune response in the adult mouse brain, while empty AAV particles did not[16,20]. This finding suggests that the DNA components of AAV vectors may act as key antigenic substances triggering immune responses. Notably, studies have shown that the AAV genome is rich in unmethylated CpG DNA, which is recognized by the innate immune system upon interacting with the Toll-like receptor 9 (TLR9) hereby activating host cells to release inflammatory cytokines and type I interferons (IFNs)[21]. Additionally, cytoplasmic DNA sensors, including the cyclic guanosine monophosphate-adenylate synthase (cGAS)−stimulator of interferon genes (STING) signaling pathway, induce the production of antiviral interferons and are crucial for recognizing and clearing viral infections[22,23]. Pharmacological inhibitors of cGAS enhance AAV transduction, while STING inhibitors mitigate AAV-induced neurotoxicity[24,25]. These studies suggest that the cGAS−STING pathway may be involved in AAV-induced immune responses in the nervous system, but its molecular mechanism has not yet been fully elucidated.

In this study, we first used bulk-RNA sequencing technology to investigate the early changes in gene expression profiles of brain tissue upon infection with different doses of AAV. Bulk RNA sequencing analysis showed that in the brains administered with 10^{10} GC AAV9, classical innate immune responses were significantly upregulated, including TLRs and NOD-like receptors (NLRs). In addition, high-dose AAV administration robustly upregulates gene expression that is involved in the cGAS−STING pathway. Using *Sting* knockout transgenic mice, we further confirmed that the cGAS−STING signaling pathway plays a crucial role in mediating inflammation, immune responses, and neuronal injury in the adult mouse brain following high-dose AAV9 intracranial injection. Further studies have found that both reactive microglia and astrocytes are involved in the activation of the cGAS−STING pathway. Microglia depletion significantly inhibited cGAS−STING pathway activation, subsequent inflammation and T cell infiltration. H-151 is a novel STING inhibitor that effectively suppressed expression of inflammatory genes, reactive glial cells, T cell infiltration and neuronal damage, while also significantly increasing the expression of transgene products delivered by AAV vectors. Altogether, our findings suggest that inhibiting the cGAS−STING pathway may improve the safety and efficacy of AAV gene therapy in the nervous system.

2. Materials and methods

2.1. Animals

Experiments were conducted on adult (2−4 months of age) wild-type C57BL/6J mice (Guangdong Yaokang Biotechnology Co., Ltd., China). Additionally, 2−3-month-old GFAP::Cre transgenic mice [B6.Cg -Tg(Gfap-cre) 77.6Mvs/2J, Cre77.6] were purchased from Jackson Laboratory, as well as Sting KO mice (Shanghai Nanmo Biotechnology Co., Ltd., China). Both male and female mice were used in this study. All mice were subjected to a standard 12-h light and dark cycle and provided with adequate water and food. Experimental protocols were approved by the Laboratory Animal Ethics Committee of Jinan University, China (approval No. IACUC-20230529-03).

2.2. AAV vector production and titering

This study primarily used AAV2/9-GFAP2.2::GFP and AAV2/9 FLEX::GFP vectors were produced by PackGene Biotech, and AAV2/11-IBA1::GFP vectors were produced by Braincase Biotech. The production process involved the following steps: First, large-scale, ultrapure plasmids were prepared and co-transfected into HEK293 cells under standard conditions. After harvesting, AAV particles were concentrated and purified through iodixanol gradient ultracentrifugation. To further improve purity and remove potential contaminating proteins or innate immune-activating factors, the viral preparations were subsequently subjected to buffer exchange and additional purification using centrifugal filter units and low-endotoxin-grade buffers. Second, the integrity of viral genomes was confirmed by specific amplification of inverted terminal repeats (ITRs) using FWD ITR and REV ITR primers, and viral titers were quantified by SYBR Green qPCR. Finally, the purity of the AAV preparations was evaluated by SDS-PAGE followed by silver staining and Coomassie staining, ensuring minimal contamination from host cell proteins or plasmid DNA. Endotoxin levels were also tested and confirmed to be below the acceptable threshold for *in vivo* use. Empty AAV9 viral capsids were prepared similarly, omitting the genomic (cis) plasmid during transfection. Their titers were determined using an AAV9-specific ELISA kit (PRAAV9, Progen). AAV titer adjustment was performed using PBS containing 0.001% F-67. The

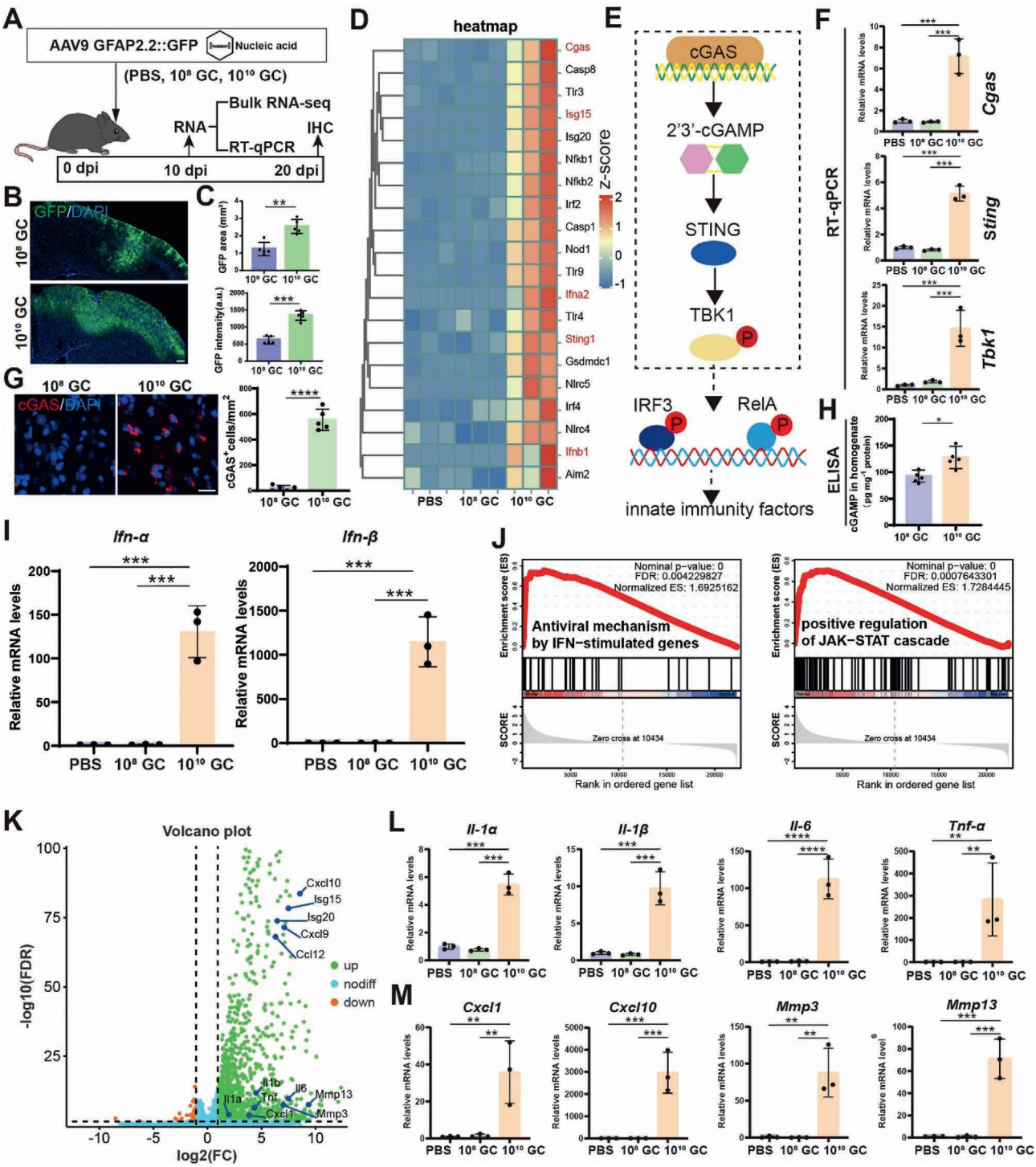

Figure 1 Bulk RNA-seq results reveal that high-dose AAV activate cGAS−STING pathway. (A) Schematic diagram of AAV injection and experimental timeline. (B) Low-power fluorescence microscopy images showing the expression of the transgene (GFP) after different doses of AAV9 were injected into the cortex. Scale bar = 200 μm. (C) The bar graphs present GFP area and intensity statistics for the 10^8 GC and 10^{10} GC groups. Values are shown as mean ± SD; $n = 5$ per group. (D) Heat map illustrating the innate immune differentially expressed genes, including Toll-like pathway genes, NOD-like pathway genes, and cGAS−STING pathway genes. (E) Schematic diagram of the cGAS−STING pathway. (F) Statistics of RT-qPCR showing the relative mRNA levels of *Cgas*, *Sting*, and *Tbk1*. Values are presented as mean ± SD; $n = 3$ per group. (G) Confocal images illustrating the cGAS signal in the 10^8 GC and 10^{10} GC groups. Scale bar = 20 μm. The bar graphs present cGAS intensity statistics for the 10^8 GC and 10^{10} GC groups. Values are shown as mean ± SD; $n = 5$ per group. (H) ELISA statistics showing the relative levels of cGAMP, which were significantly upregulated in the 10^{10} GC group. Values are presented as mean ± SD; $n = 5$ per group. (I) Statistics showing the relative mRNA levels of downstream genes in the cGAS−STING pathway, including *Ifn-α* and *Ifn-β*. Values are presented as mean ± SD; $n = 3$ per group. (J) GSEA analysis of IFN pathway and JAK-STAT pathway. (K) Volcano plot comparing the innate immune gene

AAV genome copy (GC) ranged from 10^8 to 10^{10} GC per injection. All AAVs were stored at −80 °C and used within 12 months of production.

2.3. Stereotaxic viral injection

Mice were stereotaxically injected with an AAV virus into their brains. The procedure included the following steps: First, mice were anesthetized using 20 mL/kg of 1.25% Avertin (Sigma, T48402). Next, the fur on the mice's head was shaved with a razor blade, and their scalp was cleaned with iodine tincture and ethanol. The scalp was incised with a scalpel blade, and the skull was cleaned with hydrogen peroxide before placing the mouse in a stereotaxic apparatus. Artificial eye ointment was applied to protect the eyes. A midline scalp incision was made, and a drill hole (0.5 mm) was created in the skull for virus injection into the cortex (AP +0.6 mm, ML −2 mm, DV −0.7 mm) and hippocampus (AP −2.18 mm, ML +1.5 mm, DV −1.4 mm). Using a WPI pump and glass microelectrode, 1 μL of AAV was injected into the brain at a rate of 100 nL/min. After viral injection, the glass microelectrode was left in the parenchyma for approximately 10 min before being slowly withdrawn. The mouse's scalp was sutured using surgical sutures, iodophor was applied evenly for disinfection, and the mouse was placed on a surgical heating pad to wait for recovery.

2.4. Immunofluorescence and analysis

Brain section staining involves the following steps: Mice were first anesthetized with 20 mL/kg 1.25% Avertin (Sigma, T48402), and then perfused with physiological saline or ice-cold cerebrospinal fluid. Quickly remove the brain, fix it with 4% PFA and refrigerate at 4 °C overnight.

After fixation, the samples were cut into 40 μm sections using a vibratome (Leica, VTS1200). The brain slices were washed three times in phosphate buffer for 10 min each time, during which blocking solution (5% donkey serum + 0.2% Triton X-100) was prepared. The brain slices washed with phosphate buffer solution were added to the blocking solution (5% donkey serum + 0.2% Triton X-100) for blocking for 1.5 h. To prepare the primary antibody, dilute it in blocking solution, prepare the primary antibody on an ice box according to the dilution ratio of the primary antibody (Supporting Information Table S1: primary antibody information), and incubate it in a 4 °C refrigerator for 24 h. The brain slices incubated with the primary antibody were washed three times with phosphate buffer for 10 min each time. During this period, the secondary antibody and DAPI were diluted with phosphate buffer on an ice box. This was followed by incubation with DAPI and secondary antibodies (1:1000) conjugated to Alexa Fluor 488, Alexa Fluor 555, or Alexa Fluor 647 for 2 h at room temperature. The brain slices incubated with secondary antibodies were washed three times in phosphate buffer for 10 min each time. Finally, the brain slices were affixed to glass slides and sealed with nail polish.

The images were acquired using a Zeiss confocal microscope (LSM880, Zeiss, Germany). For mice in the PBS treatment group, mouse brain slices were selected according to the injection coordinates, mouse brain atlas, and needle tract, ensuring that the selected brain slices were close to the injection site (within 300 μm). For quantification, four virus-infected regions in the cortex were randomly taken for confocal imaging (40 × lens). The images were analyzed using Zeiss software ZEN and ImageJ software.

2.5. RT-qPCR

At 4, 10 and 15 days after virus injection, we perfused the mice with ice artificial cerebrospinal fluid. Then the cortical tissue of the virus injection area (0.5 mm × 0.5 mm) was rapidly harvested and put into a 1.5 mL EP tube in bead-beating tubes containing 1 mm zirconia/silica beads (BioSpec). Tissue was homogenized for 30 s using a Mini-bead beater (BioSpec). RNA was extracted using the Rneasy Lipid Tissue Mini Kit (Cat. No. 74804). High capacity reverse transcription kit (transcriptor first strand cDNA synthesis kit) was used for cDNA synthesis. qRT-PCR was performed with SYBR green fluorescent dye of quantinova sybr green pcr kit (Cat. No. 208054). Reactions were run on a CFX96 Real-Time System (Bio-Rad Laboratories). Relative expression was calculated as $2^{-\Delta\Delta CT}$. Primer information is in Supporting Information Table S2.

2.6. Bulk RNA-seq

About Bulk RNA-seq: 10 days after virus injection, ice artificial cerebrospinal fluid was reinfused and the virus-infected center was harvested for sequencing. RNA differential expression analysis was performed by DESeq2 software between two different groups (and by edgeR between two samples). The genes/transcripts with the parameter of false discovery rate (FDR) below 0.05 and absolute fold change≥2 were considered differentially expressed genes/transcripts.

GO enrichment analysis provides all GO terms significantly enriched in DEGs compared to the genome background, and filters the DEGs that correspond to biological functions. Firstly, all DEGs were mapped to GO terms in the Gene Ontology database, and gene numbers were calculated for every term. Significantly enriched GO terms in DEGs compared to the genome background were defined by a hypergeometric test. Pathway-based analysis helps to further understand genes' biological functions. KEGG is the major public pathway-related database. Pathway enrichment analysis identified significantly enriched metabolic pathways or signal transduction pathways in DEGs compared to the whole genome background. Gene Set Enrichment Analysis (GSEA) is a gene set-based enrichment analysis method. Genes are ranked according to their relevance to sample phenotypes. Calculate the cumulative score of the gene set members. If the gene is in the set, the score is increased, otherwise the score is decreased. The final score is the enrichment score.

expression between low-dose (10^8 GC) and high-dose (10^{10} GC) AAV groups. (L, M) Statistics showing the relative mRNA levels of innate immune genes. $n = 3$ per group. A Student's *t*-test was used to evaluate the statistical significance between two groups, while one-way ANOVA with Tukey's *post hoc* test were used for comparisons among more than two groups. Significance was reported as follows: $^*P < 0.05$, $^{**}P < 0.01$, $^{***}P < 0.001$, $^{****}P < 0.0001$. ns, not significant.

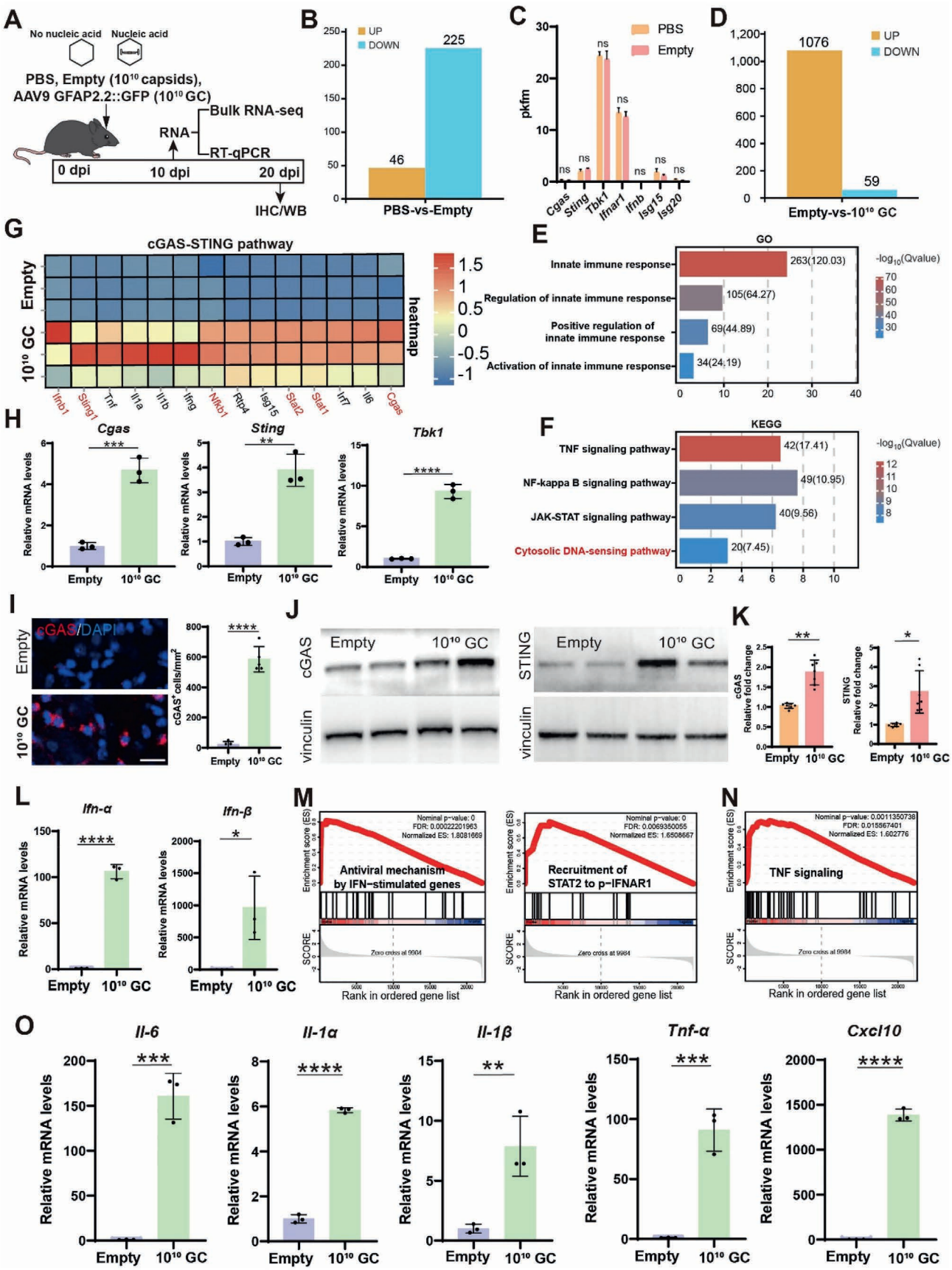

Figure 2 AAV DNA genome is necessary for cGAS−STING pathway activation. (A) Virus injection and experimental timeline. Equal volumes (1 μL) of different solutions were injected into the mouse cortex. The doses were 10^{10} capsids for empty AAV9 and 10^{10} GC for AAV9. (B) Bar

2.7. Western blot analysis

20 days after virus injection, ice artificial cerebrospinal fluid was reinfused and the virus-infected center was harvested for WB. The homogenized tissues were lysed for resolving by SDS-PAGE and transferred onto PVDF membranes (Millipore). The membrane was blocked with 5% BSA for 2 h and incubated with primary antibodies at 4 °C overnight. The membrane was washed three times in 1X TBST buffer (50 mmol/L Tris, 150 mmol/L NaCl, 0.05% Tween 20, pH 7.4) and incubated with HRP-conjugated secondary antibodies for 1.5 h at room temperature, after which the signal was detected by using an enhanced chemiluminescence.

2.8. ELISA for cGAMP detection

10 days after virus injection, ice artificial cerebrospinal fluid was reinfused and tissue from the viral infection center was collected for homogenization and cGAMP ELISA testing. ELISA was performed according to the manufacturer's protocol using the 2′-3′-cGAMP ELISA Kit (Cayman Chemical).

2.9. Cell culture and experimental design

In this experiment, two cell lines were employed: BV2 cells (purchased from Mingzhou Biotechnology Co., Ltd.) and primary mouse astrocytes. Empty AAV (10^{10} capsids) and high-dose AAV11 (10^{10} GC) were added to the BV2 cells, which were incubated for 12 h to ensure adequate viral infection. Following this incubation, the culture medium was aspirated, and the cells were washed 2−3 times to remove residual AAV from the culture dishes. Fresh culture medium was then replenished, and the cells were further incubated for 24 h. Under high-dose AAV11 infection of BV2, an additional ENPP1 (50 μmol/L) treatment group was added, according to a previous study[26]. After incubation, the supernatant was collected *via* centrifugation for cGAMP ELISA analysis or was transferred to dishes containing astrocytes for a 48 h co-culture period, followed by immunohistochemical (IHC) analysis.

Primary astrocyte isolation and culture: the cortices from postnatal Day 2−3 mice were dissected and enzymatically digested with 0.15% trypsin-EDTA (a 1:1 mixture of 0.05% trypsin-EDTA and 0.25% trypsin-EDTA) for 15 min. The resulting cell suspension was then plated in non-coated culture flasks for expansion, using a medium composed of DMEM/F12 (supplemented with 4.5 g/L glucose and 2 mmol/L L-glutamine), 10% fetal bovine serum (FBS, sourced from Australia), and 1% penicillin/streptomycin, and incubated in a 5% CO_2 atmosphere at 37 °C (all reagents from Thermo Fisher Scientific, Grand Island, NY, USA). After 7−9 days, when the cells reached approximately 90% confluence, non-astrocytic cells (including microglia, neurons, oligodendrocytes, and their progenitors) were removed by gentle agitation, and the remaining astrocytes were reseeded in astrocyte maintenance medium containing DMEM/F12 (supplemented with 3.5 mmol/L glucose, 2 mmol/L L-glutamine), 2% B27, 10% FBS, and 1% penicillin/streptomycin.

2.10. Microglia depletion by PLX5622

To pharmacologically eliminate brain microglia, the mice were fed with PLX5622-formulated AIN-76A diet (1.2 g PLX5622 per kilogram of diet) *at libitum*. In contrast, the control mice were fed the normal AIN-76A diet (control diet, CD) *ad libitum*. Then perform immunohistochemistry and RT-qPCR.

2.11. The treatments of H-151

Immediately after virus injection, the mice were intraperitoneally injected with STING inhibitor H-151 (1, 3 and 10 mg/kg, S6652, Selleck) once every two days. The H-151 administration cycle is 10 days, and then RT-qPCR is performed. The H-151 administration cycle is 30 days, and then perform immunohistochemistry.

2.12. Data and code availability

The bulk RNA-seq datasets supporting the results of this article have been deposited in Gene Expression Omnibus (GSE311583) database and are publicly available from the date of publication of this article. All of the plasmids used in this study are available from the lead contact upon request.

2.13. Statistical analysis

The quantification data were expressed as mean ± standard deviation (SD). Statistical analysis was performed by the unpaired Student's *t*-test and one-way ANOVA analysis with Tukey's *post hoc* test. Differences were considered statistically significant at $P < 0.05$. Significant differences are indicated by $^{*}P < 0.05$, $^{**}P < 0.01$, $^{***}P < 0.001$, and $^{****}P < 0.0001$. ns, not significant.

graphs showing DEGs in PBS and empty groups. (C) Statistics showing the pkfm levels of innate immune genes in PBS and empty groups. (D) Bar graphs showing DEGs in empty and 10^{10} GC groups. There were more than 1000 DEGs between the empty group and 10^{10} GC group. (E) GO-enriched bar graphs indicating that the 10^{10} GC group induced a strong innate immune response in the mouse brain. (F) KEGG-enriched bar graphs demonstrating that the 10^{10} GC group elicited innate immune responses, including type I interferon upstream cGAS−STING pathway (cytosolic DNA-sensing pathway) and NF-kappa B signaling pathway/JAK−STAT signaling pathway. (G) The heat map showing DEGs in the cGAS−STING pathway. (H) RT-qPCR statistics showing relative mRNA levels of *Cgas, Sting*, and *Tbk1* genes, which were dramatically upregulated in the 10^{10} GC group. Values are shown as mean ± SD; $n = 3$ per group. (I) Confocal images showing the cGAS signal in empty and 10^{10} GC groups. Scale bar = 20 μm. The bar graph (right) is the density of $cGAS^{+}$ cell in the empty and 10^{10} GC groups. Values are shown as mean ± SD; $n = 5$ per group. (J, K) Western blot results and statistics of cGAS and STING protein expression in the AAV injected brain regions. The molecular weights of cGAS, STING, and vinculin are 62, 35, and 117 kDa, respectively. $n = 7$ mice per group. (L) RT-qPCR statistics showing relative mRNA levels of type1 interferon genes *Ifn-α* and *Ifn-β*. At 10^{10} GC group both were dramatically upregulated. Values are shown as mean ± SD; $n = 3$ per group. (M, N) GSEA analysis of IFN pathway, JAK−STAT pathway and TNF-α pathway. (O) RT-qPCR quantified bar graphs showing relative mRNA levels of innate immune genes. $n = 3$ per group. A Student's *t*-test was used to evaluate the statistical significance between two groups. Significance reported as: $^{*}P < 0.05$, $^{**}P < 0.01$, $^{***}P < 0.001$, $^{****}P < 0.0001$. ns, not significant.

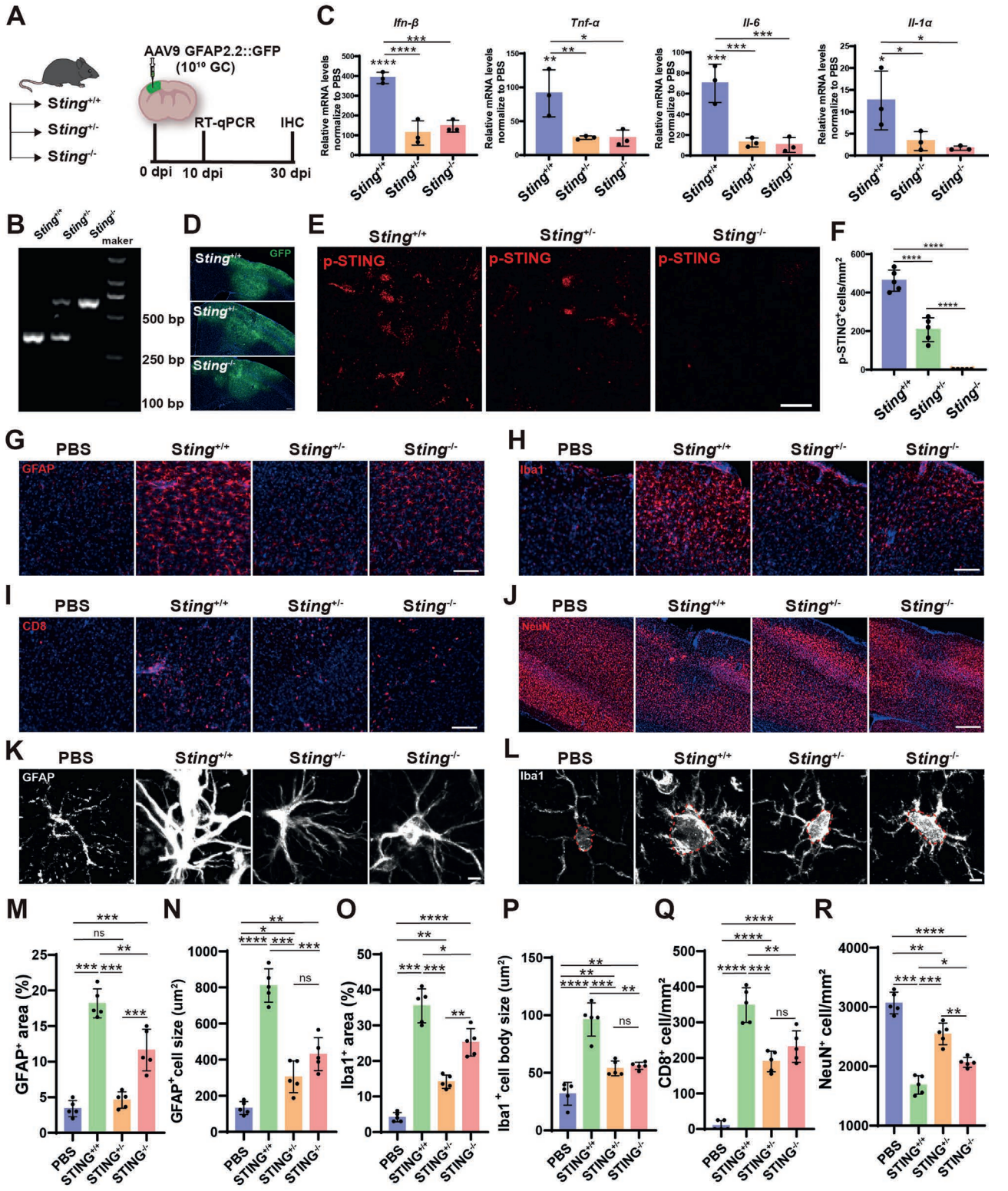

Figure 3 *Sting* knockout transgenic mice reveal the role of the cGAS−STING pathway in high-dose AAV induced innate immunity. (A) The experimental design for *Sting* knockout transgenic mice. (B) Genotyping results confirming the successful knockout of the *Sting* gene in transgenic mice. (C) RT-qPCR analysis of innate immune gene expression, including *Il-6*, *Il-1β*, *Tnf-α*, and *Ifn-β*, in high-dose AAV9 treated (*Sting*$^{+/+}$, *Sting*$^{+/-}$, and *Sting*$^{-/-}$) mice. Notably, the expression of these genes was significantly diminished in both homozygous and heterozygous *Sting* knockout mice following injection with 10^{10} GC AAV9. The relative mRNA changes were normalized to the PBS group. $n = 3$ per group. (D) Low magnification fluorescence microscope images display the expression of transgene (AAV9-GFP) in *Sting*$^{+/+}$, *Sting*$^{+/-}$, and *Sting*$^{-/-}$ mice. Scale bar = 200 μm. (E) Confocal images reveal the p-STING signal in *Sting*$^{+/+}$, *Sting*$^{+/-}$, and *Sting*$^{-/-}$ mice. Scale bar = 20 μm. (F) Quantifications of p-STING $^{+}$ cell numbers are shown in *Sting*$^{+/+}$, *Sting*$^{+/-}$, and *Sting*$^{-/-}$ mice. $n = 5$ per group. (G−J) Low-

3. Results

3.1. AAV intraparenchymal injection activates the cGAS−STING pathway in a dose-dependent manner

To investigate the innate immune response to intraparenchymal injection of AAV in adult mouse brain, we selected two doses of AAV9 which are comparable to clinical trials[12,27,28]. Then, 10^8 GC (1 μL × 10^{11} GC/mL; Low) and 10^{10} GC (1 μL × 10^{13} GC/mL; High) of AAV vectors were directly injected into the mouse cortex, and the same volume of PBS was used as a vehicle control. Following stereotaxic injection, mouse cortices were harvested at 10 days post injection (dpi) for bulk RNA-Seq and RT-qPCR analysis, 20 dpi for immunohistochemistry (IHC) studies (Fig. 1A). First, to assess the AAV9 transduced region, we utilized the human glial fibrillary acidic protein promoter (GFAP2.2), which is commonly employed to drive transgene expression in astrocytes, to express the green fluorescent protein (GFP) in these cells. Our results showed that both the GFP fluorescence intensity and the transduction area were significantly greater in the high-dose group compared to the low-dose group (Fig. 1B and C). Second, bulk RNA sequencing (RNA-seq) was employed to assess the impact of different AAV9 doses on gene expression in the injected cortical region. As expected, genes related to the Toll-like receptor and NOD-like receptor pathways, including *Tlr9*, *Tlr2*, *Nod2*, and *Nlrp3*, were sharply upregulated in the high-dose group (Fig. 1D). In addition, genes enrolled in the cGAS−STING pathway such as *Cgas*, *Sting* and *Ifnb1*, were also dramatically enhanced in the high-dose group (Fig. 1D). The basic process of the cGAS−STING signaling pathway starts with abnormal DNA sensing and binding in the cytosol by cGAS, followed by synthesizing the cyclic GMP−AMP (cGAMP), which then binds and activates STING on the endoplasmic reticulum. Subsequently, TBK1 and IRF3 are activated to induce the expression of IFNs and interferon-stimulated genes (Fig. 1E)[22,29]. Gene Ontology (GO) enrichment analysis found that many differentially expressed genes (DEGs) were enriched in biological processes related to DNA damage (Supporting Information Fig. S1A), which may activate the DNA sensor cGAS. RT-qPCR further confirmed that the core genes of the cGAS−STING pathway (*Cgas*, *Sting*, and *Tbk1*) were significantly upregulated in the high-dose group (Fig. 1F). Furthermore, immunofluorescence staining for cGAS revealed a substantial increase in cGAS signals in the high-dose group compared to the low-dose group (Fig. 1G). Activated cGAS catalyzes the formation of the second messenger cGAMP, so we performed an ELISA test and found that the cGAMP level in the tissue homogenate injected with high-dose of AAV9 was significantly increased (Fig. 1H). Together, these data suggest that while high-dose AAV9 can achieve efficient transgene expression in the brain, it also activates the cGAS−STING pathway, potentially triggering an inflammatory response.

cGAS−STING signaling pathway activation results in the release of inflammatory cytokines and IFNs[30,31]. Using RT-qPCR, we observed that *Ifn-α* and *Ifn-β*, were dramatically upregulated by hundreds to thousands of times in the high-dose group compared with the PBS and low-dose groups (Fig. 1I). Moreover, Gene Set Enrichment Analysis (GSEA) analysis indicated the activation of the type I interferon pathway and its downstream JAK−STAT pathway (Fig. 1J). Further investigation using volcano plots and RT-qPCR revealed that high-dose AAV9 significantly upregulated the expression of interferon-stimulated genes (ISGs), including *Isg15* and *Isg20* (Fig. 1K). Notably, this upregulation was accompanied by the concurrent activation of numerous downstream innate immune factors within the cGAS−STING pathway. For example, our RT-qPCR data showed a significant increase in the expression of interleukin family members, including *Il-1α*, *Il-1β*, and *Il-6*, as well as tumor necrosis factor *Tnf-α* (Fig. 1L). Additionally, we observed increased expression of chemokines, such as *Cxcl1* and *Cxcl10*, and metalloproteinases (MPP), including *Mmp3* and *Mmp13* (Fig. 1M). These findings collectively suggest that high-dose AAV9 triggers a robust innate immune response characterized by the activation of the cGAS−STING pathway.

3.2. DNA genome in AAV capsid is necessary for cGAS−STING pathway activation

cGAS is a cytoplasmic DNA sensor, we assessed whether the DNA within the AAV is required for activation of the cGAS−STING pathway[29,32]. To this end, empty AAV9 viral capsids (10^{10} capsids) without genomic DNA were used. The high-dose of empty AAV9 and genome-containing AAV9 vectors were injected into the mouse cortex, respectively. The total mRNAs of the injected area were extracted at 10 dpi for bulk RNA-seq and RT-qPCR analysis, samples were collected at 20 dpi for IHC and Western Blot (WB) study (Fig. 2A). We first compared the DEGs between the PBS group and the empty AAV9 group, and found 271 DEGs (Fig. 2B and Supporting Information Fig. S2A). Notably, no DEGs were involved in the cGAS−STING pathway (Fig. 2C), but were related to the extracellular matrix biological process (Fig. S2B). However, genome-containing AAV9 injection elicited substantial transcriptome alterations, encompassing over thousands of DEGs when compared to empty AAV9 group (Fig. 2D). GO enrichment analysis revealed that these DEGs were enriched in biological processes related to innate immunity (Fig. 2E). Further KEGG analysis indicated that these DEGs were enriched in the inflammatory responses and cytosolic DNA-sensing pathways, which may be related to the activation of the cGAS−STING pathway (Fig. 2F). Accordingly, the heatmap generated from the DEGs further demonstrated that genes within the cGAS−STING pathway including *Cgas*, *Sting*, *Ifnb1*, *Nfkb1*, and *Stat1* were upregulated in genome-containing AAV9 compared to empty AAV9 treated mice (Fig. 2G). RT-qPCR further confirmed the significant upregulation of core genes involved in the cGAS−STING pathway (*Cgas*, *Sting*, and

magnification Zeiss fluorescence microscope images display the GFAP (G), Iba1 (H), CD8 (I), and NeuN (J) signals in S*ting*$^{+/+}$, S*ting*$^{+/-}$, and S*ting*$^{-/-}$ mice after injection of 10^{10} GC AAV9. Scale bar = 100 μm. (K, L) High-magnification images show a typical astrocyte (K) and microglia (L) in different groups. The red circle in panel L indicates the cell body of the microglia. (M, N) Quantifications of GFAP positive cell area proportion and average cell size that are shown in PBS, S*ting*$^{+/+}$, S*ting*$^{+/-}$, and S*ting*$^{-/-}$ mice. (O, P) Quantifications of the percentage of Iba1$^+$ area and average cell soma size in different groups. (Q) Quantifications of CD8$^+$ cell numbers are shown in PBS, S*ting*$^{+/+}$, S*ting*$^{+/-}$, and S*ting*$^{-/-}$ mice. (R) Quantifications of NeuN$^+$ cell numbers are shown in PBS, S*ting*$^{+/+}$, S*ting*$^{+/-}$, and S*ting*$^{-/-}$ mice. Values are shown as mean ± SD; $n = 5$ per group. One-way ANOVA analysis with Tukey's *post hoc* test. Significance reported as: $^*P < 0.05$, $^{**}P < 0.01$, $^{***}P < 0.001$, $^{****}P < 0.0001$. ns, not significant.

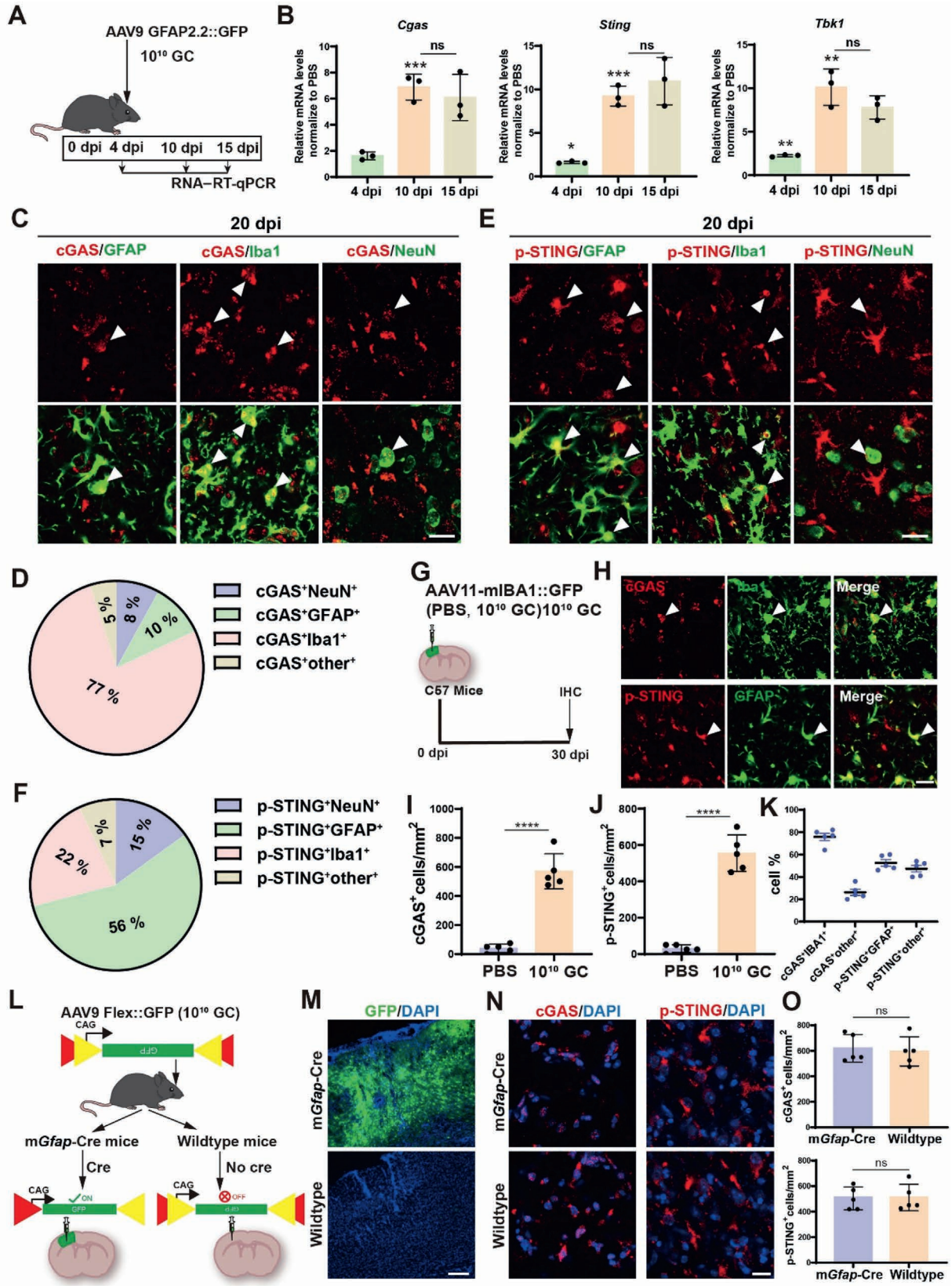

Figure 4 Activation of cGAS−STING pathway in microglia and astrocytes independent of GFP expression. (A) Experimental timeline for virus injection and RT-qPCR analysis. (B) RT-qPCR statistics showing relative mRNA levels of *Cgas*, *Sting*, and *Tbk1* genes at 4, 10, and 15 dpi. $n = 3$ per group. (C) Confocal images of cGAS (red, pseudocolor) co-stained with GFAP (green, pseudocolor), NeuN (green, pseudocolor), and Iba1 (green, pseudocolor) at 20 dpi following injection of 10^{10} GC AAV9. Arrowheads indicate the typical cells expressing cGAS. Scale

Tbk1) when mice were injected with normal AAV9 (Fig. 2H). Furthermore, immunofluorescence staining confirmed that there was no cGAS signal in the empty AAV9 group, while abundant cGAS expression was observed in the cortex injected with the normal AAV9 at 20 dpi (Fig. 2I). Our Western blot analysis further revealed that the expression levels of both cGAS and STING were significantly elevated in mice treated with normal AAV9 compared to those treated with empty AAV9 (Fig. 2J and K).

The cGAS−STING signaling pathway is a critical mediator of antiviral responses, facilitating the induction of type I interferons and interferon-stimulated genes[33,34]. Consistently, our RT-qPCR analysis revealed a significant upregulation of both *Ifn-α* and *Ifn-β* in the normal AAV9 group (Fig. 2L). Furthermore, GSEA analysis confirmed the activation of the type I interferon pathway and tumor necrosis factor (TNF) pathway in tissues injected with normal AAV9 (Fig. 2M and N). Again, RT-qPCR validation also demonstrated the significant upregulation of downstream innate immune genes, including interleukin family factors (*Il-6*, *Il-1α*, and *Il-1β*), *Tnf-α* and the chemokine *Cxcl10* (Fig. 2O). Taken together, the DNA genome within the AAV9 capsid is necessary for inducing the activation of the cGAS−STING pathway.

3.3. cGAS−STING pathway contributes significantly to AAV-induced innate immunity

To evaluate the contribution of the cGAS−STING pathway in the innate responses induced by AAV9 intraparenchymal injection, the *Sting* knockout mice were employed in this study. We prepared littermate mice with 3 genotypes including $Sting^{+/+}$ (wild type, WT), $Sting^{+/-}$ (heterozygous), and $Sting^{-/-}$ (homozygous). Then 10^{10} GC of AAV9 was injected into the cortex, and RT-qPCR analysis was *performed* at 10 dpi, while IHC studies were conducted at 30 dpi (Fig. 3A and B). The results revealed that downstream genes of cGAS−STING pathway, including *Ifn-α*, *Ifn-β*, *Il-6* and *Il-1β*, were significantly reduced both in heterozygous and homozygous, suggesting that *Sting* deficiency alleviated AAV9 induced innate immunity (Fig. 3C). IHC results demonstrated that the transgene GFP in AAV9 vectors was highly expressed in the cortices of mice from all three genotypes (Fig. 3D). We also examined the phosphorylated STING (p-STING, activated form) in different genotyping mice after injection of AAV9 and found that the p-STING was significantly reduced in heterozygous mice and completely lost in the homozygous mice (Fig. 3E and F). Of note, despite p-STING reaching undetectable levels in homozygous mice, the effectors of the innate response (*IFN-α*, *IFN-β*, *IL-6* and *IL-1β*) induced by AAV9 were not significantly different between heterozygous and homozygous mice (Fig. 3C), suggesting that *Sting* haploinsufficiency is sufficient to inhibit cGAS−STING pathway activation.

Immune activation in the CNS involves astrocytes and microglia[35,36], so we wondered whether *Sting* deficiency would affect the activation of astrocytes and microglia. Reactive astrocyte and microglia were revealed by GFAP and Iba1 immunostaining, respectively. Administration of 10^{10} GC of AAV9 induced a significant upregulation of GFAP and Iba1 expression in WT mice (Fig. 3G and H). However, this upregulation was substantially attenuated in both heterozygous and homozygous mice, with the degree of reduction being notably more pronounced in heterozygous mice (Fig. 3G and H; Quantified in Fig. 3M and O), suggesting a genotype-dependent modulation of the glial reactivation. Furthermore, astrocyte hypertrophy and microglia swelling were detected after intracerebral injection of high doses of AAV9 in WT mice, while these phenomena were significantly reduced in $Sting^{+/-}$ and $Sting^{-/-}$ mice (Fig. 3K and L; Quantified in Fig. 3N and P). Activation of the cGAS−STING signaling pathway can attract and activate a variety of immune cells, including T cells, especially $CD8^+$ T cells, which are the main killer cells of neurons[37,38]. Thus, we examined cytotoxic T cell ($CD8^+$) infiltration in brain parenchyma after high-dose AAV9 injection, and found that the infiltrated $CD8^+$ T cells were significantly reduced in both heterozygous and homozygous mice (Fig. 3I, quantified in Fig. 3Q). Consequently, infiltration of $CD8^+$ T cells into brain parenchyma resulted in neuronal damage in WT mice, however, this side effect was significantly alleviated in both heterozygous and homozygous mice. To our surprise, quantitative analysis revealed a significant reduction in the extent of neuronal loss in heterozygous mice compared to their homozygous littermates (Fig. 3J, quantified in Fig. 3R). Collectively, these data suggest that targeting cGAS−STING pathway inhibits high-dose AAV9 induced glia reactivation, $CD8^+$ T cell infiltration and neuronal damage.

3.4. cGAS−STING pathway activation in microglia and astrocyte

To investigate spatiotemporal activation patterns of the cGAS−STING pathway in the brain, we first assessed transcriptional changes using RT-qPCR following high-dose AAV9 administration (Fig. 4A). Time-course analysis revealed a

bar = 20 μm. (D) The pie chart showing 77% of $cGAS^+$ cells containing Iba1, 10% of $cGAS^+$ cells containing GFAP and 8% of $cGAS^+$ cells containing NeuN in the total $cGAS^+$ cell population. (E) Confocal images of STING (red) co-stained with GFAP, NeuN, and Iba1 at 20 dpi following injection of 10^{10} GC AAV9. Arrowheads indicate the typical cells expressing p-STING. Scale bar = 20 μm. (F) Pie chart illustrating the distribution of $STING^+$ cells: 22% of $STING^+$ cells are $Iba1^+$, 56% are $GFAP^+$, and 15% are $NeuN^+$. (G) Schematic diagram of the virus injection protocol and experimental timeline. (H) Confocal images showing cGAS (red, (green, pseudocolor) co-stained with Iba1 (green, pseudocolor) and STING (red, pseudocolor) co-stained with GFAP (green, pseudocolor) at 30 dpi in AAV11-injected mice. Arrowheads indicate a typical microglia (top) and astrocytes (bottom) expressing cGAS and p-STING, respectively. Scale bar = 20 μm. (I, J) Cell density quantification of $cGAS^+$ and $STING^+$ cells in PBS treated and AAV11 treated mice, regardless of cell type. $n = 5$ per group. (K) Quantification showing the cell type specific proportions of $cGAS^+$ and p-$STING^+$ cells. $n = 5$ per group. (L) Diagram illustrating the Cre-Flex system, where GFP expression is regulated by Cre recombinase. (M) Low magnification images displaying GFP (green) signals. GFP expression was detected in the m*Gfap*-Cre transgenic mouse brain, while no GFP signal was observed in wild-type mice. Scale bar = 200 μm. (N) Confocal images revealing cGAS and STING signals in m*Gfap*-Cre transgenic and wild-type mice. (O) Quantification of $cGAS^+$ and $STING^+$ cell populations in m*Gfap*-Cre transgenic and wild-type mice. Data are presented as mean ± SD ($n = 5$ per group). A Student's *t*-test was used to evaluate the statistical significance between two groups, while one-way ANOVA with Tukey's *post hoc* test were used for comparisons among more than two groups. Significance is indicated as: $^*P < 0.05$, $^{**}P < 0.01$, $^{***}P < 0.001$, $^{****}P < 0.0001$. ns, not significant.

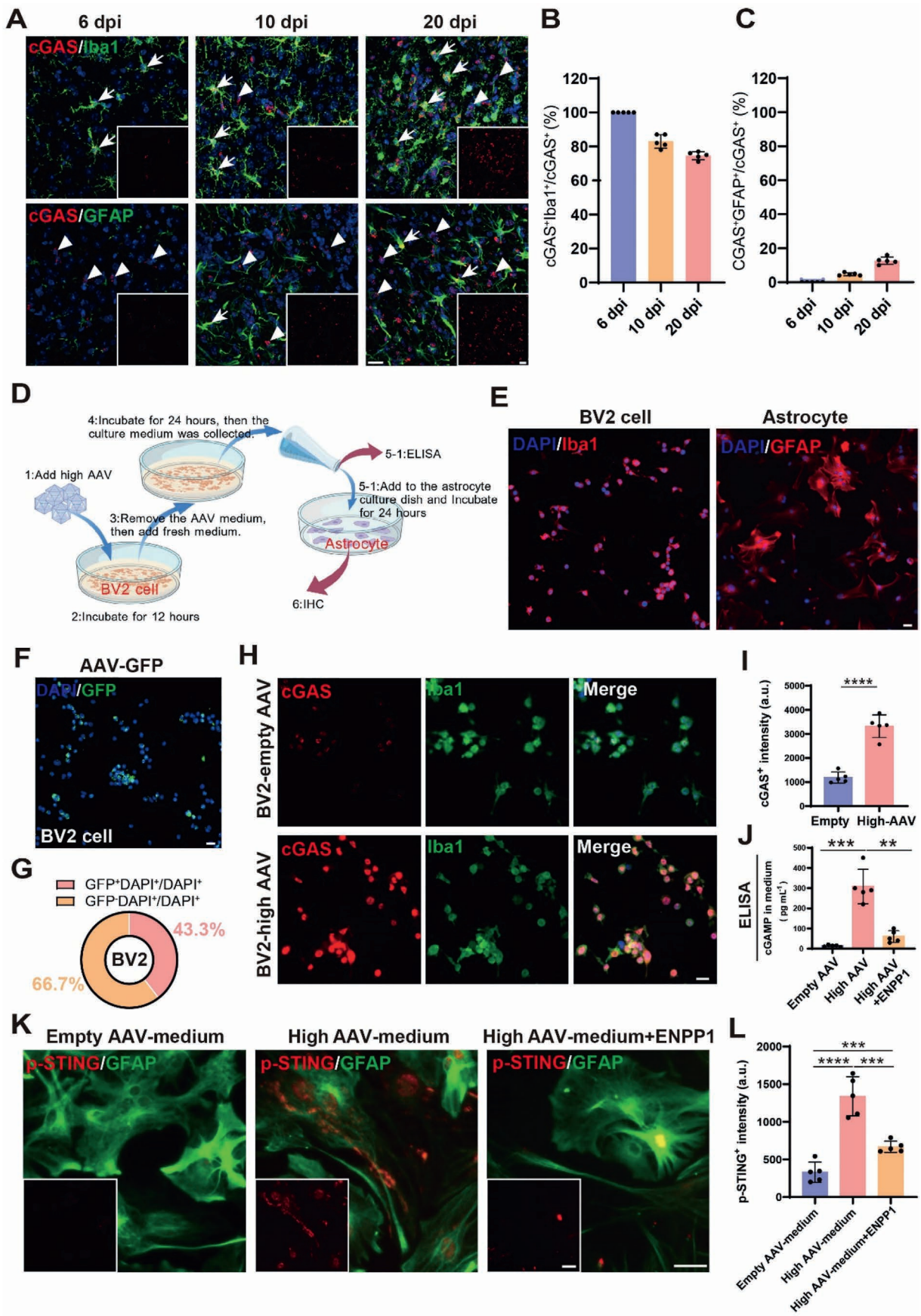
A
6 dpi
10 dpi
20 dpi
cGAS/Iba1
cGAS/GFAP
B
cGAS+Iba1+/cGAS+ (%)
6 dpi
10 dpi
20 dpi
C
CGAS+GFAP+/cGAS+ (%)
6 dpi
10 dpi
20 dpi
D
4:Incubate for 24 hours, then the culture medium was collected.
1:Add high AAV
3:Remove the AAV medium, then add fresh medium.
BV2 cell
2:Incubate for 12 hours
5-1:ELISA
5-1:Add to the astrocyte culture dish and Incubate for 24 hours
Astrocyte
6:IHC
E
BV2 cell
Astrocyte
DAPI/Iba1
DAPI/GFAP
F
AAV-GFP
DAPI/GFP
BV2 cell
G
GFP+DAPI+/DAPI+
GFP-DAPI+/DAPI+
43.3%
66.7%
BV2
H
BV2-empty AAV
BV2-high AAV
cGAS
Iba1
Merge
I
cGAS+ intensity (a.u.)
****
Empty
High-AAV
J
ELISA
cGAMP in medium (pg mL-1)
***
**
Empty AAV
High AAV
High AAV +ENPP1
K
Empty AAV-medium
High AAV-medium
High AAV-medium+ENPP1
p-STING/GFAP
L
p-STING+ intensity (a.u.)
***
****
***
Empty AAV-medium
High AAV-medium
High AAV-medium+ENPP1

significant upregulation of *Cgas*, *Sting*, and *Tbk1* transcripts at 4 dpi, with a more robust increase by 10 dpi. These elevated expression levels persisted through the 15-days observation period (Fig. 4B). Moreover, to identify specific cellular contributors to pathway activation, we conducted co-immunofluorescence staining with cell-type markers at 20 dpi. Although GFP expression was primarily localized to astrocytes (Supporting Information Fig. S3A−S3C), cGAS immunoreactivity predominantly occurred in microglia (77%), with limited detection in astrocytes (10%) and neurons (8%) (Fig. 4C and D). Conversely, p-STING signals concentrated in astrocytes (56%), with lower levels in microglia (22%) and neurons (15%) (Fig. 4E and F). These findings establish microglia and astrocytes as the principal responders to AAV9-induced cGAS−STING activation in the adult mouse brain.

As resident myeloid immune cells of the CNS, microglia represent potential targets for neurological gene therapies[39,40]. However, whether microglial-tropic AAV serotypes also activate the cGAS−STING signaling pathway remains unknown. Building on our findings with AAV9, we next examined AAV11, a recently developed serotype with strong microglial tropism[41], to further investigate how vector-specific cellular targeting influences cGAS−STING mediated innate immune responses in the mouse brain. To this end, 10^{10} GC of AAV11-IBA1::GFP vectors were directly injected into the mouse cortex and samples were collected at 30 dpi (Fig. 4G). We found that the transgene (GFP) in AAV11 was expressed in microglia with a specificity of 97% (Fig. S3D−S3H). Compared to PBS, cGAS signal was dramatically upregulated in microglia following intraparenchymal injection of AAV11 (Fig. 4H top and Fig. 4I). Interestingly, although GFP was not expressed in astrocytes, p-STING immune signals were also detected in astrocytes (Fig. 4H bottom), and the number of p-STING$^+$ cells was tremendously increased (Fig. 4J). Quantitative analysis revealed that approximately 80% of cGAS$^+$ cells were identified as microglia (Iba1$^+$), whereas nearly 60% p-STING$^+$ cells were found to be astrocytes (GFAP$^+$, Fig. 4K). Together, these data suggest that AAV11, which specifically targets microglia, can also activate the cGAS−STING pathway in astrocytes and microglia.

To determine whether cGAS−STING pathway activation requires transgene expression following high-dose AAV9 administration, we implemented a Cre-dependent system (AAV9-Flex-CAG::GFP) in astrocyte-specific m*Gfap*-Cre transgenic mice (Cre77.6 line) versus wild-type controls (Fig. 4L). This strategy enables GFP expression exclusively in Cre-expressing astrocytes. As expected, robust GFP fluorescence appeared in m*Gfap*-Cre mice but remained undetectable in wild-type animals (Fig. 4M), confirming strict Cre-dependent transgene regulation. Strikingly, cGAS and STING showed comparable upregulation in AAV9-exposed brain regions irrespective of GFP expression status (Fig. 4N). Quantitative analysis revealed equivalent cGAS and p-STING levels between GFP-expressing and non-expressing conditions (Fig. 4O). These findings indicated that cGAS−STING pathway activation occurs independently of transgene expression in AAV9-mediated CNS delivery.

3.5. Interaction between microglia and astrocytes during cGAS−STING pathway activation

Since both cGAS and p-STING signals were detected in microglia and astrocytes, we aimed to determine which cell type was the first to respond following high-dose AAV administration. Mouse cortices were injected with high-dose AAV9 (10^{10} GC), and mice were sacrificed at 2, 6, 10, and 20 dpi for immunostaining analysis (Supporting Information Fig. S4A). Our results showed that reactive microglia, characterized by an increased cell body size, were detectable as early as 6 dpi (Fig. S4B and S4C), whereas hypertrophic astrocytes were first observed at 10 dpi (Fig. S4D and S4E). Alongside these morphological changes, the density of cGAS$^+$ cells gradually increased in regions transduced by high-dose AAV9 (Fig. S4F and S4G). Notably, at 6 dpi, all cGAS signals were localized to microglia (Iba1$^+$), while only a small number of astrocytes (GFAP$^+$) exhibited detectable cGAS immunoreactivity at 10 dpi (Fig. 5A). Moreover, microglia remained the predominant cell type, constituting over 75% of all cGAS$^+$ cells at 20 dpi (Fig. 5B), with astrocytes accounting for less than 15% (Fig. 5C). These findings suggest that microglia are the first and most dominant cell type to activate the cGAS−STING signaling pathway following high-dose AAV9 injection.

cGAS is an enzyme that catalyzes the synthesis of cGAMP, a second messenger molecule. After high-dose AAV infection, cGAS was predominantly found in microglia. Our next goal was to investigate whether cGAMP synthesized in microglia can be released and transferred to astrocytes, thereby activating the STING protein. To test this, we cultured BV2 cells, a mouse-derived microglial cell line, and primary mouse astrocytes *in vitro* (Fig. 5D). Nearly 100% of the cultured BV2 cells and primary astrocytes were labeled with Iba1 and GFAP, respectively (Fig. 5E). Twelve hours after infection with AAV11-IBA1::GFP, 43.3% of BV2 cells expressed GFP (Fig. 5F and G). Compared to the empty AAV treatment group, we observed a higher intensity of

Figure 5 Microglia release cGAMP and transferred to astrocyte. (A) Confocal images show cGAS co-stained with Iba1 (microglia) and GFAP (astrocytes) at different time points after high-dose AAV11 injection. Arrows indicate cells expressing both signals, while the arrowheads indicate cells only expressing cGAS. Pseudocolors were used. Scale bar = 20 μm. (B, C) Bar graphs show the proportion of microglia (B) and astrocytes (C) in cGAS $^+$ cells. $n = 5$ per group. (D) Schematic illustrating BV2 cell and astrocyte culture experiments and study design. (E) Immunostaining images show that cultured BV2 cells and astrocytes are co-stained with microglia and astrocyte markers Iba1 and GFAP, respectively. Scale bar = 20 μm. (F) Representative images of BV2 cell cultures transduced with AAV11 (GFP$^+$). Scale bar = 20 μm. (G) The pie chart shows that 43.3% of BV2 cells express GFP. (H) Representative confocal images of co-immunostained cGAS (red, pseudocolor) and Iba1 (green, pseudocolor) cells in cultured BV2 cells treated with empty AAV capsids (top) or high-dose AAV-GFP (bottom). Scale bar = 20 μm. (I) cGAS fluorescent intensity was significantly increased in high-dose AAV treated BV2 cells. $n = 5$ per group. (J) The concentration of cGAMP in BV2 cell conditioned medium that treated under different conditions. $n = 5$ per group. (K) Immunostaining of GFAP (green, pseudocolor) and p-STING (red, pseudocolor) in primary astrocytes cultured with different conditioned media. Scale bar = 20 μm. (L) Fluorescent intensity of p-STING in cultured astrocyte. $n = 5$ per group. Data are shown as mean ± SD. A Student's *t*-test was used to evaluate the statistical significance between two groups, while one-way ANOVA with Tukey's *post hoc* test were used for comparisons among more than two groups. Significance is indicated as: $^{**}P < 0.01$, $^{***}P < 0.001$, $^{****}P < 0.0001$. ns, not significant.

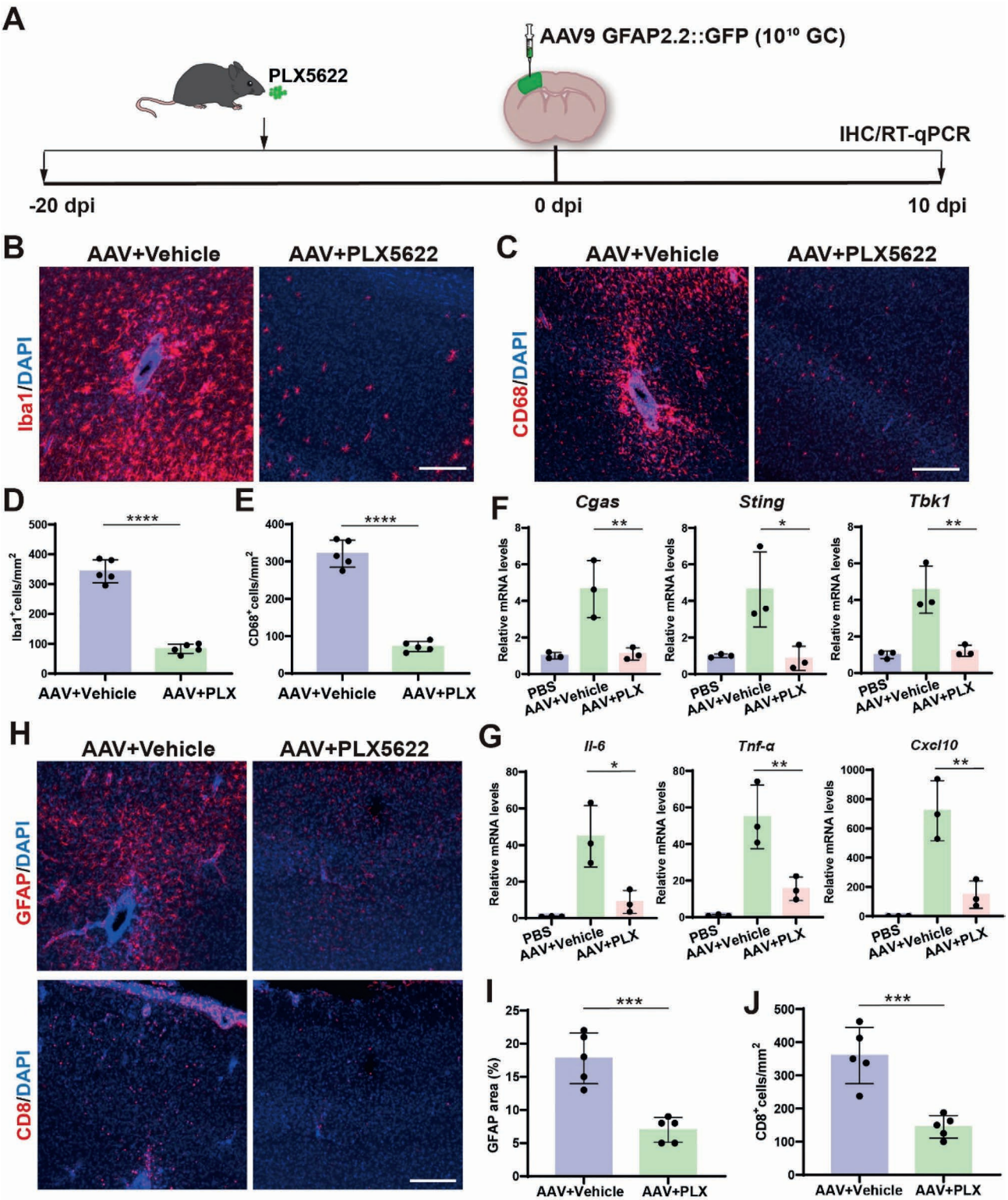

Figure 6 Microglia depletion alleviates AAV9-induced innate immune responses. (A) Schematic representation of the experimental design for microglia depletion. (B, C) Low magnification confocal images displaying Iba1 (a pan-microglia marker) and CD68 (an activated microglia marker) in the cortex of AAV9 injected mice treated with either vehicle or PLX5622. Scale bar = 200 μm. (D, E) Quantifications of $Iba1^+$ and $CD68^+$ cell numbers in vehicle and PLX5622 groups. Values are shown as mean ± SD; $n = 5$ per group. (F, G) RT-qPCR analysis revealing the relative mRNA levels of innate immune genes *Cgas*, *Sting*, *Tbk1*, *Il-6*, *Tnf-α*, and *Cxcl10* in the PBS, vehicle, and PLX5622 treatment groups. Results indicate that PLX5622 effectively attenuates innate immune responses. Data are presented as mean ± SD; $n = 3$ per group. (H) Low magnification confocal images of GFAP and CD8 in the cortex of AAV9 injected mice treated with vehicle and PLX5622, respectively. PLX5622 treatment significantly reduces astrocyte activation and $CD8^+$ T cell infiltration. Scale bar = 200 μm. (I, J) Quantification of GFAP intensity and

cGAS fluorescent signal in the high-dose AAV group (Fig. 5H and I). ELISA assays further confirmed that the cGAMP concentration in the culture medium of high-dose AAV-treated BV2 cells was significantly increased, while it was markedly reduced after the addition of cGAMP hydrolase ENPP1 (50 μmol/L, Fig. 5J). These results provide strong evidence that high-dose AAV treatment induces cGAMP production in BV2 cells and release to the culture medium.

Subsequently, we transferred the conditioned medium from high-dose AAV treated or empty AAV treated (control) BV2 cells into wells containing astrocytes. After 24 h of co-culturing, the conditioned medium from the high-dose AAV group significantly enhanced p-STING signaling in astrocytes (Fig. 5K and L). However, the addition of ENPP1 to the conditioned medium significantly reduced cGAMP, which in turn resulted in a marked decrease in p-STING signaling in the astrocytes (Fig. 5K and L). Taken together, these data demonstrate that cGAMP, produced in microglia upon high-dose AAV infection, is transferred to astrocytes, where it activates STING signaling.

3.6. Microglia depletion effectively inhibits activation of cGAS−STING pathway

Since cGAS signaling is primarily detected in microglia, we investigated whether microglia depletion in the mouse brain would impact the immune response triggered by high-dose AAV9. Mice were fed with PLX5622 diet (1.2 g PLX5622 per kilogram of diet), a widely used small molecule for microglial depletion[42], for 20 days. Subsequently, high-dose AAV9 was injected into the mouse cortex, and the mice continued to receive PLX5622 diet for an additional 10 days, then immunostaining and RT-qPCR analyses were performed (Fig. 6A). We first assessed the effect of PLX5622 on the number of microglia in the cortex following PBS or high-dose AAV9 injection. Microglial depletion was confirmed by Iba1 staining of mouse brain sections, which revealed a significant reduction in microglial numbers in both groups treated with PLX5622. Notably, while high-dose AAV9 injection resulted in a marked increase in $Iba1^+$ cells in the cortex, PLX5622 significantly inhibited this increase (Fig. 6B, quantified in Fig. 6D). CD68, a well-established macrophage marker primarily located in microglia within the brain parenchyma, is often used as an indicator of microglial activation and immune response to tissue damage. Consistent with the Iba1 staining, the increase in $CD68^+$ microglia induced by high-dose AAV9 was significantly attenuated by PLX5622 treatment (Fig. 6C and E). Furthermore, microglia depletion with PLX5622 substantially abolished the upregulation of key cGAS−STING pathway genes (*Cgas*, *Sting*, and *Tbk1*, Fig. 6F) as well as their downstream effectors (*Il-6*, *Tnfα*, and *Cxcl10*, Fig. 6G) induced by high-dose AAV9. Additionally, PLX5622 treatment significantly reduced astrocyte activation, evidenced by decreased GFAP expression (Fig. 6H top, quantified in Fig. 6I) and $CD8^+$ T cell infiltration following high-dose AAV9 injection (Fig. 6H bottom, quantified in Fig. 6J). Collectively, these findings demonstrate a critical role for microglia in regulating the cGAS−STING signaling cascade and subsequent immune responses in the context of high-dose AAV9 administration.

3.7. Pharmacological inhibition of the cGAS−STING pathway attenuates high-dose AAV9-induced immune responses in adult mouse brain

To explore the potential of modulating the cGAS−STING pathway to mitigate the immune response triggered by high-dose AAV9, we utilized a brain permeable STING inhibitor H-151[43,44]. Following high-dose AAV9 injection, we administered STING inhibitor H151 to pharmacologically inhibit STING activation as previously reported in other neurological disorders[45,46]. We treated mice with H-151 intraperitoneally (i.p.) every other day at varying doses (1, 3, and 10 mg/kg) to evaluate dose-dependent effects on subsequent biological responses (Fig. 7A). RT-qPCR analysis revealed that treatment with H-151 at 10 mg/kg significantly reduced the expression of innate immune inflammatory cytokines, including *Il-6*, *Il-1α*, and *Tnf-α*, as well as type I interferon *Ifn-β*, a key downstream target of the cGAS−STING pathway (Fig. 7B). These findings demonstrate that pharmacological inhibition of STING using the small-molecule compound H-151 effectively attenuates high-dose AAV9 induced activation of the cGAS−STING signaling pathway and expression of downstream effector genes.

Our previous study showed that 30 days after high-dose AAV9 injection, massive glial reactivation and immune cell infiltration occurred at the injection site, accompanied by severe neuronal loss[16]. Therefore, we injected 10 mg/kg H-151 intraperitoneally every other day until the 30th day after 10^{10} GC of AAV9 injection, and the control group mice received the same volume of vehicle (Fig. 7C). Immunofluorescence staining of the neuronal marker NeuN revealed substantial neuronal loss in the vehicle group (injected with high-dose AAV9) compared to the PBS group. However, H-151 treatment at 10 mg/kg significantly reduced neuronal loss after injection of high-dose AAV9 (Fig. 7D and E). Inhibition of the cGAS−STING pathway by H-151 also effectively alleviated microglia and astrocyte activation, as well as $CD8^+$ T cell infiltration (Fig. 7F−I). Furthermore, H-151 treatment markedly enhanced both the expression levels and spatial distribution range of the AAV9 reporter GFP (Fig. 7J and K). To evaluate the effects of H-151 in other brain regions, we injected high-dose AAV9 into the hippocampus and treated with H-151 in the same manner as in the cortex. Similar to the cortex, H-151 treatment reduced neuronal loss, alleviated glial reactivation and immune cell infiltration in the hippocampus (Supporting Information Fig. S5). Together, these observations indicate that H-151 treatment significantly reduces neuronal loss, alleviates glial reactivation and immune cell infiltration induced by high-dose AAV9 injection, without affecting transgene expression.

3.8. H-151 effectively alleviated inflammation and neuronal loss in the retina

The eye, like the brain, is an immune-privileged organ, making it an ideal target for AAV-mediated gene therapy. However, studies have demonstrated that AAV can induce inflammation and immune cell infiltration in the retina in a dose-dependent manner[21,47]. To investigate whether the cGAS−STING signaling pathway is involved in high-dose AAV9-induced retinal

$CD8^+$ cell numbers in the vehicle and PLX5622-treated groups. Data are presented as mean ± SD; $n = 5$ per group. A Student's *t*-test was used to evaluate the statistical significance between two groups, while one-way ANOVA with Tukey's *post hoc* test were used for comparisons among more than two groups. Significance reported as: $^*P < 0.05$, $^{**}P < 0.01$, $^{***}P < 0.001$, $^{****}P < 0.0001$. ns, not significant.

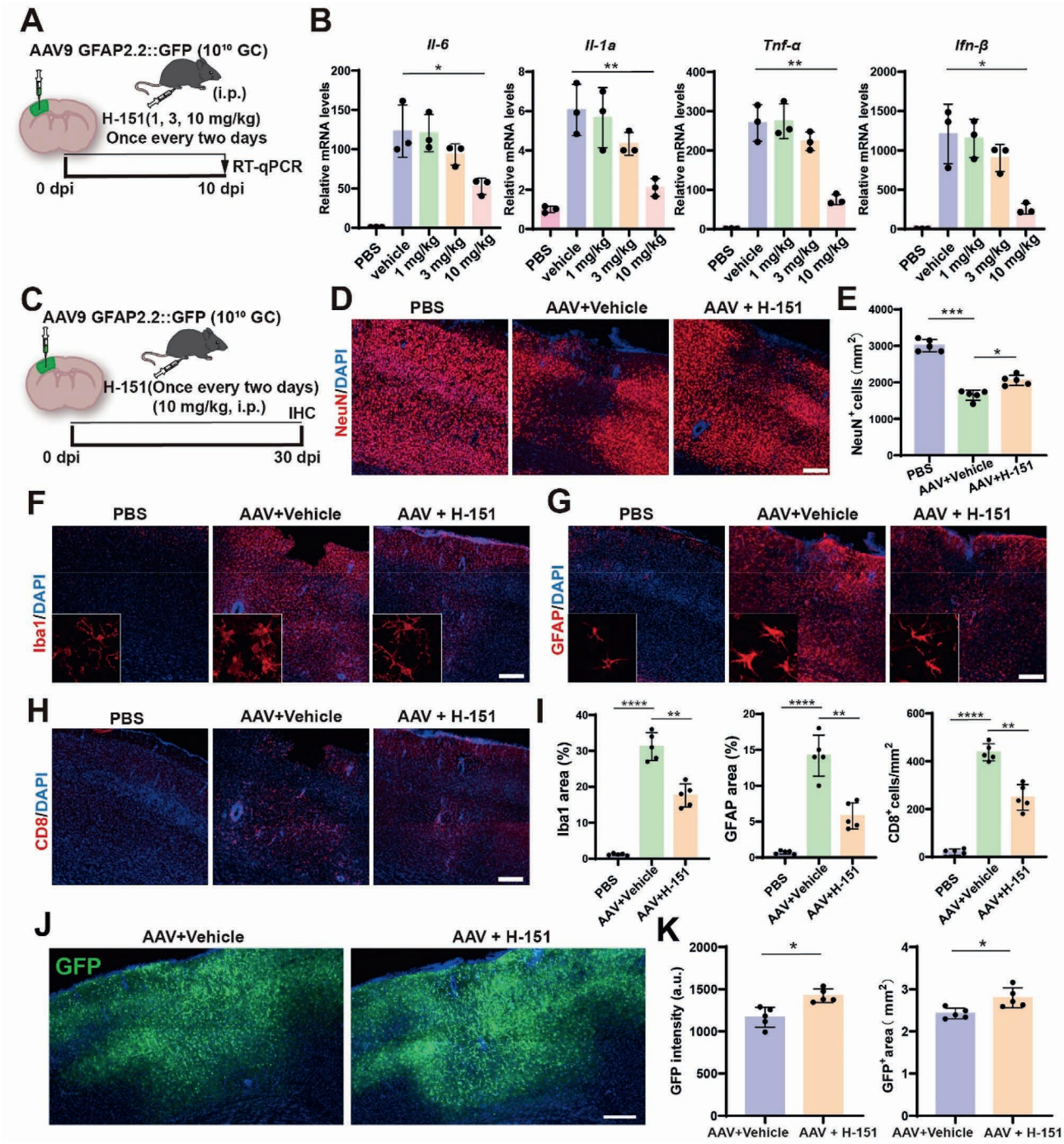

Figure 7 H-151 inhibits the STING pathway and reduces immunity and neuronal Loss. (A) Experimental design for virus injection and H-151 drug administration. Three distinct doses of H-151 were selected to evaluate its efficacy. (B) RT-qPCR statistics show relative mRNA levels of innate immune genes (*Il-6*, *Il-1α*, *Tnf-α*, *Ifn-β*) in PBS, AAV + vehicle and AAV + H-151 groups. The results indicate that 10 mg/kg H-151 effectively reduces inflammatory factors. Data are presented as mean ± SD; $n = 3$ per group. (C) Experimental design for virus injection and administration of 10 mg/kg H-151. (D) Representative confocal images showing NeuN (red) labeling in mice treated with PBS (left), AAV + vehicle (middle), and AAV + H-151 (right, 10 mg/kg). Scale bar = 200 μm. (E) Quantification of neuron counts, revealing a significant rescue of neuronal density following administration of the STING inhibitor H-151. (F) Low magnification images of GFAP immunostaining in the cortex of mice treated with PBS, AAV + vehicle, and AAV + H-151 (10 mg/kg). Scale bar = 200 μm. (G) Low magnification images of Iba1 immunostaining in the cortex of mice treated with PBS, AAV + vehicle, and AAV + H-151 (10 mg/kg). Scale bar = 200 μm. (H) Low magnification images showing infiltrated $CD8^+$ T cells in the mouse cortex from three different groups. Scale bar = 200 μm. (I) Quantification results indicating that H-151 treatment significantly reduces microglial and astrocytic reactivation, as well as $CD8^+$ T cell infiltration. Data are presented as mean ± SD; $n = 5$ per group. (J) Low magnification images showing GFP expression in the adult mouse cortex following treatment with AAV + vehicle or AAV + H-151. (K) Quantification of GFP intensity and coverage area in the AAV + vehicle and AAV + H-151 groups.

inflammation and immune responses, we injected 10^{10} GC of AAV9 into the subretinal space of the adult mouse eyes, with PBS serving as the sham control. Additionally, some mice receiving 10^{10} GC of AAV9 were treated with the STING inhibitor H-151 (10 mg/kg, i.p.), while others were given an equal volume of vehicle as a control. Retinas from the mice were then collected for RT-qPCR and immunohistochemistry analysis (Fig. 8A). RT-qPCR results (10 dpi) showed that 10^{10} GC of AAV9 administration in the retina activated the cGAS−STING signaling pathway (*Cgas*, *Sting* and *Tbk1*, Fig. 8B), resulting in a significant upregulation of downstream antiviral and inflammatory-associated gene expression (*Il-6*, *Il-1α* and *Ifn-β*, Fig. 8C). Immunofluorescence staining at 30 dpi revealed a significant increase in p-STING$^+$ cells following subretinal injection of high-dose AAV9, with predominant expression in retinal GFAP$^+$ cells, primarily astrocytes and reactive Müller cells (Fig. 8D). Notably, pharmacological inhibition of STING with H-151 substantially attenuated these antiviral and inflammatory responses, with mRNA levels of target genes reduced by 45%−55% compared to vehicle treated controls (Fig. 8C). These findings suggest that the cGAS−STING signaling pathway plays a significant role in high-dose AAV9 induced inflammation in the mouse retina.

To evaluate whether H-151 could inhibit high-dose AAV induced glial reactivation, T cell infiltration and neuronal loss by inhibiting the cGAS−STING pathway, we collected samples (30 dpi) for further histomorphological studies (Fig. 8A). High-dose AAV9 caused retinal thinning, which was revealed by nuclear staining (DAPI), while H-151 treatment could not rescue the retinal thinning caused by high-dose AAV9 subretinal injection (Fig. 8E and F). Interestingly, staining with the retinal glial marker GFAP and Iba1 showed that although H-151 could not restore overall retinal thickness, it effectively inhibited glial reactivation and CD8$^+$ T cell infiltration (Fig. 8G−K). Subsequently, we performed immunostaining for NeuN, a typical neuronal marker expressed in the retina primarily on retinal ganglion cells (RGCs), which are the only cells in the visual pathway that can send electrical output signals to the brain. We found that after subretinal injection of high-dose AAV9, RGCs in mice receiving vehicle administration significantly degenerated. However, RGCs were significantly protected from high-dose AAV9 induced neuronal toxicity by H-151 (Fig. 8L and M). Overall, our study shows that inhibition of the cGAS−STING pathway has the potential to improve the safety of AAV9-mediated ocular gene therapy.

4. Discussion

In this study, we designed experiments using low and high-doses of AAV to investigate the effects of cGAS−STING-mediated innate immune responses on the nervous system. By bulk-RNA sequencing, RT-qPCR, and histochemical analysis, we demonstrated that high-doses of AAV induce activation of the cGAS−STING pathway. RNA Sequencing and histochemical results provided convincing evidence that AAV nucleic acid is indeed necessary to initiate activation of the cGAS−STING pathway. Immunostaining results indicated that microglia and astrocytes were the main effector cells of high-dose AAV activated cGAS−STING pathway. Using STING knockout transgenic mice, we confirmed that high-dose AAV activated cGAS−STING pathway plays a crucial role in immune responses and neuronal loss. Depletion of microglia by PLX5622 effectively inhibited the expression of inflammation-related genes and T cell infiltration. In addition, the STING inhibitor H-151 was used to block the cGAS−STING signaling pathway, effectively reducing glial reactivation, immune cell infiltration and neuronal damage caused by high-dose AAV, while also increasing the expression area and intensity of the transgene. Together, this study reveals cGAS−STING activation as the cause of dose-dependent neuroinflammation in AAV9 based nervous system gene therapy and suggests that STING inhibition may provide a clinically feasible approach to optimize the safety-effectiveness balance in gene delivery.

Adeno-associated virus (AAV) vectors have emerged as one of the most promising tools for gene therapy due to their ability to deliver therapeutic genes efficiently with relatively low immunogenicity[2,48]. However, despite their advantages, the use of AAV vectors is not without challenges, particularly regarding the potential for adverse immune responses[1,49]. These immune responses not only limit the efficacy of AAV gene therapy but may also lead to severe side effects, such as hepatobiliary diseases, and in some cases, even result in patient mortality[7,9,50]. Over the years, significant progress has been made in understanding the side effects of AAV gene therapy, which include innate immune activation, T cell infiltration, and glial reactivation[15,16,19,20]. Recent studies have provided valuable insights into the molecular mechanisms underlying these responses, highlighting the role of pattern recognition receptors such as TLRs and RIG-I in initiating immune activation upon AAV exposure[18,21,49,51]. Of note, in 2019, Laurel and colleagues reported elevated cGAS and STING expression in response to retinal gene transfer using AAV vectors, with drug interventions enhancing transduction efficiency[24]. This implies that the cGAS−STING pathway plays a role in AAV-induced immune responses. More recently, a study suggested the involvement of the cGAS−STING pathway in the p53-dependent DNA damage response triggered by AAV genomes in a human iPSC-derived CNS model[25]. Together with our current findings in the adult mouse nervous system, these studies indicate that cGAS−STING is a critical innate immune regulator, contributing significantly to AAV-induced inflammation and neurotoxicity. This highlights its potential as a therapeutic target for mitigating AAV-related neurotoxicity.

cGAS is a crucial DNA sensor that activates immune responses upon detecting both pathogen and self-DNA. A recent study using human iPSC-derived brain organoids demonstrated that AAV genomes trigger a p53-dependent DNA damage response, potentially activating cGAS[25]. However, this study did not examine the gene expression changes within the cGAS−STING pathway, and the absence of microglia, the brain's major resident immune cells, limits its ability to model the immune response accurately[31,52]. Although STING inhibitors reduced AAV-induced inflammation and neurotoxicity, the underlying molecular mechanisms remain unclear, highlighting the need for further research in more physiologically relevant models. In this study, we aimed to elucidate

Both GFP intensity and coverage area were significantly increased upon treatment with the STING inhibitor H-151. Values are shown as mean ± SD; $n = 5$ per group. A Student's *t*-test was used to evaluate the statistical significance between two groups, while one-way ANOVA with Tukey's *post hoc* test were used for comparisons among more than two groups. Significance reported as: $^*P < 0.05$, $^{**}P < 0.01$, $^{***}P < 0.001$, $^{****}P < 0.0001$. ns, not significant.

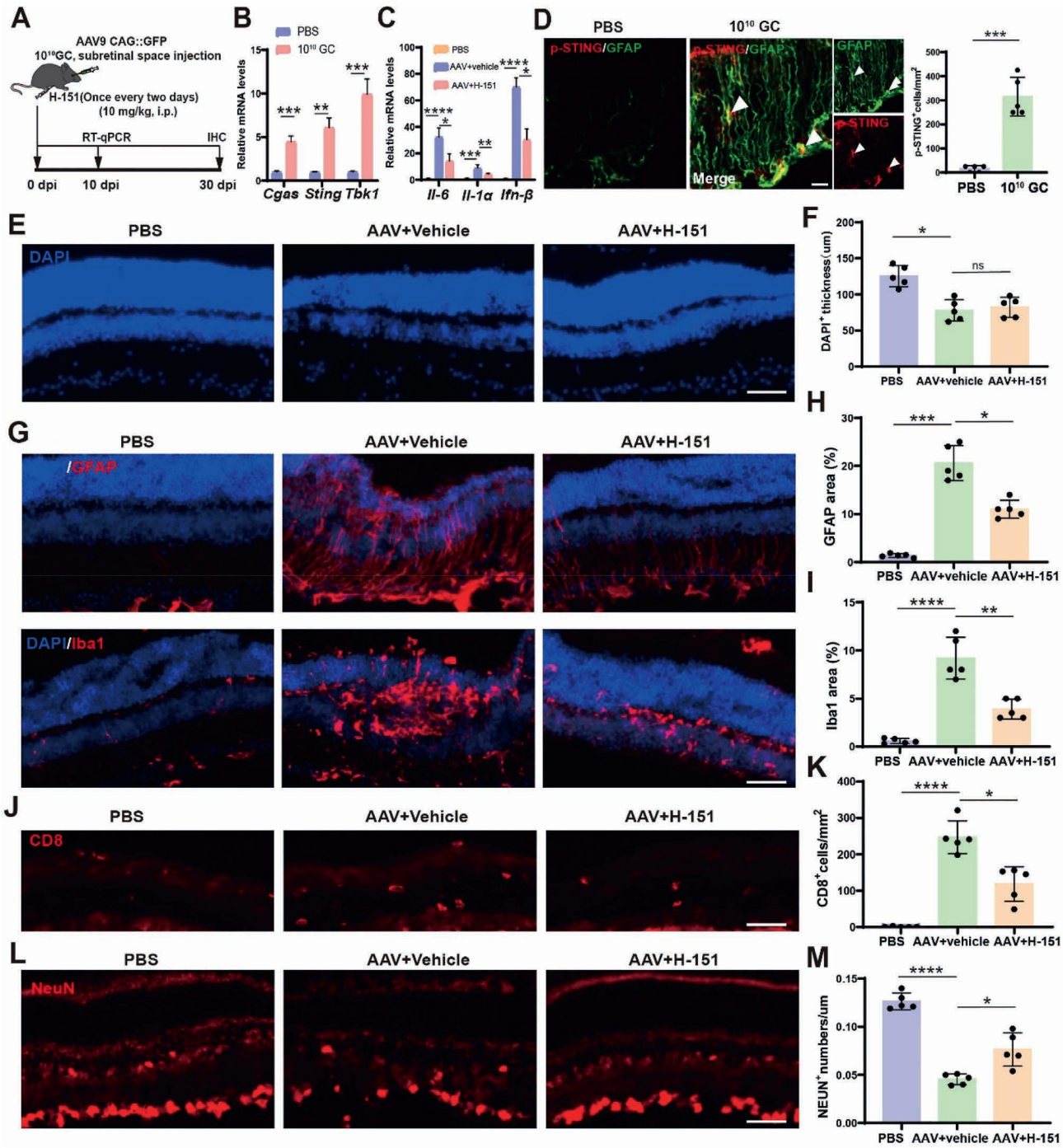

Figure 8 H-151 reduces inflammation and neuronal loss in the retina after subretinal AAV9 injection. (A) Experimental design: The virus was injected subretinally, while H-151 was administered intraperitoneally. (B) RT-qPCR analysis of relative mRNA expression levels of cGAS−STING pathway genes (*Cgas*, *Sting*, and *Tbk1*) in PBS and 10^{10} GC groups. $n = 3$ per group. (C) RT-qPCR analysis of innate immune gene expression, including *Il-6*, *Il-1α*, and *Ifn-β*, in PBS, vehicle, and H-151 treated groups. $n = 3$ per group. (D) Confocal images showing p-STING (red, pseudocolor) co-localized with GFAP (green, pseudocolor) at 30 dpi and quantification of p-STING $^{+}$ cell numbers in PBS and 10^{10} GC groups. Arrowheads indicate GFAP $^{+}$ cells expressed p-STING. Scale bar = 20 μm. (E, G, J, L) Low magnification fluorescence images from a Zeiss microscope displaying DAPI (blue, E), GFAP (G, top), Iba1 (G, bottom), CD8 (J), and NeuN (L) signals in PBS, AAV + vehicle, and AAV + H-151 treated groups. Scale bar = 50 μm. (F, H, I, K, M) Quantification of DAPI positive layer thickness (F), the percentage of GFAP covered area (H), the percentage of Iba1 covered area (I), $CD8^{+}$ cell counts (K), and $NeuN^{+}$ cell counts (M). Data are presented as mean ± SD ($n = 5$ per group). A Student's *t*-test was used to evaluate the statistical significance between two groups, while one-way ANOVA with Tukey's *post hoc* test were used for comparisons among more than two groups. Significance levels are indicated as: $^{*}P < 0.05$, $^{**}P < 0.01$, $^{***}P < 0.001$, $^{****}P < 0.0001$. ns, not significant.

the mechanism underlying the activation of the cGAS−STING pathway in the adult mouse brain upon AAV transduction. Our findings reveal that microglia are the primary cell type responsible for cGAS activation, while astrocytes predominantly activate STING (p-STING). These observations are consistent with the established roles of these cell types as key immune mediators in the central nervous system[31,35,40,53]. Our results underscore the critical involvement of microglia in initiating the cGAS−STING signaling cascade, as demonstrated by the predominant detection (77%) of cGAS protein in Iba1$^+$ cells. This may be attributed to the fact that, following AAV transduction, the AAV genome does not efficiently enter the microglial cell nucleus[54]. By selectively depleting microglia in the adult mouse brain using the small molecule PLX5622, we observed a marked reduction in cGAS−STING pathway activation following high-dose AAV administration, providing strong evidence for the critical role of microglia in this process. Interestingly, we observed that over half of the p-STING (56%) was localized to astrocytes, suggesting that the cGAS−STING pathway may not operate exclusively within a single cell type (*e.g.*, microglia or astrocytes), but rather involves intercellular communication. Specifically, cGAMP, as an important second messenger, is mainly synthesized by cGAS in microglia and is transferred to astrocytes, where it activates STING. This intercellular transfer of cGAMP has been reported in other cell types by previous studies[55-57]. Once inside astrocytes, cGAMP activates STING in the endoplasmic reticulum, leading to the induction of type I interferons and interferon-stimulated genes, thereby amplifying the immune response. While this hypothesis offers a comprehensive framework for understanding the crosstalk between microglia and astrocytes in the activation of the cGAS−STING pathway, further experimental investigations are needed to fully validate these findings.

Our study reveals that intracerebral injection of high-dose AAV activates the cGAS−STING signaling pathway, which is accompanied by significant neuronal loss at the injection site. The activation of the cGAS−STING pathway triggers inflammation, recruits immune cells, and promotes the migration and activation of adaptive immune cells, which may contribute to neuronal death[16]. In addition, a recent study has further indicated that following STING activation, a non-canonical pathway can induce neuronal autophagy, leading to the degradation of GPX4 and the activation of ferroptosis[58]. To further investigate the role of STING in this process, we injected high-dose AAV9 into the brains of STING knockout transgenic mice. Surprisingly, complete deletion of STING did not substantially reduce the neuronal loss induced by high-dose AAV9. In contrast, we observed the most significant reduction in neuronal death in STING heterozygous knockout mice. This finding may be attributed to the multifaceted physiological functions of STING. Recent studies have shown that STING, as a proton channel, plays a role in lysosome biogenesis and autophagy regulation[59,60]. In addition to its well-known functions in mediating cGAS responses or stimulating autophagy, nuclear STING is also involved in the transcriptional regulation of specific genes[61]. Furthermore, our bulk RNA sequencing data further suggest that the inflammation induced by high-dose AAV is not solely mediated by the cGAS−STING pathway. Other pathways, such as Toll-like receptors and NOD-like receptors, are also significantly upregulated. Notably, our bulk RNA sequencing analysis also revealed a significant upregulation of key genes in the AIM2/caspase-1/GSDMD inflammasome pathway following high-dose AAV9 injection into the adult mouse brain. This pathway is a critical component of the innate immune response, acting as a cytoplasmic sensor for intracellular DNA[62,63]. The activation of this inflammasome, alongside the cGAS−STING pathway, suggests that high-dose AAV9 may trigger multiple innate immune responses related to nucleic acid sensing in neurons. These findings highlight the potential for AAV9-mediated neurotoxicity through the activation of distinct but interconnected DNA sensing pathways, underscoring the need to further investigate the role of inflammasome-driven pyroptosis in AAV-induced brain inflammation. Therefore, complete knockout of the *Sting* gene, which blocks the cGAS−STING pathway, does not fully eliminate the innate immune response driven by above alternative pathways[15,17,49]. Moreover, complete deletion of STING may increase the sensitivity of other innate immune signaling pathways, leading to compensatory increases in inflammation and immune responses. Thus, our results highlight that the *Sting* heterozygous knockout mice, which retain one copy of the *Sting* gene, provide the most effective neuronal protection, suggesting a complex interplay between STING and other immune signaling pathways. In the future, the development of a novel STING modulator could offer a more potent neuroprotective effect compared to a complete STING blocker.

In our retinal model, H-151 reduced inflammation and neuronal loss caused by high-dose AAV9 injection, yet it did not prevent retinal thinning. This discrepancy could be attributed to several factors. While H-151 effectively modulates the cGAS−STING pathway to reduce immune-mediated inflammation, AAV9-mediated retinal damage involves complex mechanisms beyond immune activation. Specifically, AAV9 gene therapy can induce structural changes in the retina, including mechanical stress, vascular alterations, and non-immune toxicity, which may contribute to retinal thinning[64-66]. For example, the mechanically stress-sensitive ion channel Piezo1 is expressed in various retinal cell types, and a recent study demonstrated that its overactivation can lead to cell damage in retina[67]. The inability of H-151 to prevent retinal thinning suggests that while inflammation plays a critical role in neuronal loss, it may not be the primary driver of tissue structural damage in this context. This highlights the need to consider other factors, such as the direct effects of AAV9 on retinal vasculature or the mechanical strain imposed by viral vector delivery, which may not be addressed by STING inhibition alone. Future research should explore these additional mechanisms and investigate combination therapies that target both immune and non-immune pathways to better preserve retinal integrity in gene therapy applications.

While this study provides valuable insights into the activation of the cGAS−STING signaling pathway by AAV vectors, several aspects require further investigation. First, although we have demonstrated that the presence of DNA within the AAV capsid is essential for activating the cGAS−STING pathway, we have not directly shown that AAV genomic DNA itself serves as the direct substrate for cGAS activation. Additionally, the current model relies on single-stranded DNA AAV vectors, whereas cGAS recognizes double-stranded DNA. It remains unclear whether the single-stranded DNA released from AAV particles needs to undergo reverse transcription to form double-stranded DNA for subsequent cGAS activation. This raises the possibility that alternative mechanisms, such as the formation of episomal DNA, could also contribute to cGAS activation[48,49]. Furthermore, while TLR9 has been well-established to recognize unmethylated CpG motifs commonly found in pathogenic viral and bacterial DNA[21,68], it remains uncertain whether cGAS exhibits a similar

sequence preference for specific DNA motifs within the AAV genome. Recent studies on human brain organoids have suggested that AAV transduction can trigger early DNA damage responses, potentially involving host genomic DNA damage in cGAS activation[25]. However, whether this is a direct or indirect consequence of AAV transduction requires clarification. Therefore, future research should aim to further elucidate the molecular mechanisms underlying high-dose AAV-induced activation of the cGAS−STING pathway, with a particular focus on the interaction between AAV vector DNA and the host immune sensing machinery. In addition, this study provides preliminary insights, but the dosing regimen of H-151 (10 mg/kg every other day) requires further optimization. Future work should include pharmacokinetic analyses, including bioavailability, brain penetration, and target engagement, as well as dose-response and time-course studies to better inform clinical translation. Overall, such studies could provide crucial insights for improving AAV-based gene therapy vectors and enhancing the safety and efficacy of gene therapy strategies.

5. Conclusions

In conclusion, our findings highlight the critical role of the cGAS−STING pathway in mediating the innate immune response to high-dose AAV, and that its inhibition using the STING inhibitor H-151 effectively mitigates associated inflammation and innate immune activation. Specifically, H-151 treatment not only reduced the expression of proinflammatory cytokines and type I interferon, but also promoted the expression of the transgene. These results suggest that targeting the cGAS−STING pathway may be a viable strategy for reducing AAV immunogenicity and enhancing its therapeutic potential. Moreover, our study provides new insights into the mechanisms underlying the immune response to AAV and underscores the potential of STING inhibition as a therapeutic approach for mitigating adverse immune reactions. Overall, our findings have important implications for the development of AAV-based therapies and suggest that further investigation into the role of the cGAS−STING pathway in AAV-mediated immunity is warranted.

Acknowledgments

The work was funded by the National Natural Science Foundation of China to Zheng Wu (No. 82571603), the Program for Guangdong Introducing Innovative and Entrepreneurial Teams to Zheng Wu and Gong Chen (Grant No. 2021ZT09Y552, China), the Pearl River Talent Program Youth Outstanding Project to Zheng Wu (0920220219, China), and the Fundamental Research Funds for the Central University to Zheng Wu (21625111, China).

Author contributions

Zheng Wu, Gong Chen and Wenliang Lei conceived and supervised the entire project. Yaowei Guo performed all experiments with assistance from Jiehao Huang, Yuqi Zhang, Yuxiang Huang, Zeru Li, Yingqi Cao, Kun Qian, and Fan Bai. Dr. Wen Li provided constructive comments during manuscript preparation. Yaowei Guo and Zheng Wu analyzed the data, made the figures, and wrote the manuscript.

Conflicts of interest

Gong Chen is a co-founder of NeuExcell Therapeutics Inc. The remaining authors declare no competing interests.

Appendix A. Supporting information

Supporting information to this article can be found online at https://doi.org/10.1016/j.apsb.2026.04.001.

References

1. Ling Q, Herstine JA, Bradbury A, Gray SJ. AAV-based *in vivo* gene therapy for neurological disorders. *Nat Rev Drug Discov* 2023;**22**: 789−806.
2. Wang JH, Gessler DJ, Zhan W, Gallagher TL, Gao GP. Adeno-associated virus as a delivery vector for gene therapy of human diseases. *Signal Transduct Tar* 2024;**9**:78.
3. Tong F, Li H, Gao H, Li Y. Engineered tumor specific AAV for IL-12 delivery in ovarian cancer immunotherapy. *Acta Pharm Sin B* 2025;**15**: 4316−8.
4. Yang P, Pardon LP, Ho AC, Lauer AK, Yoon D, Boye SE, et al. Safety and efficacy of ATSN-101 in patients with Leber congenital amaurosis caused by biallelic mutations in GUCY2D: a phase 1/2, multicentre, open-label, unilateral dose escalation study. *Lancet* 2024;**404**:962−70.
5. Pasi KJ, Rangarajan S, Mitchell N, Lester W, Symington E, Madan B, et al. Multiyear Follow-up of AAV5-hFVIII-SQ gene therapy for Hemophilia A. *N Engl J Med* 2020;**382**:29−40.
6. Lv J, Wang H, Cheng XT, Chen YX, Wang DQ, Zhang LL, et al. AAV1-hOTOF gene therapy for autosomal recessive deafness 9: a single-arm trial. *Lancet* 2024;**403**:2317−25.
7. Duan D. Lethal immunotoxicity in high-dose systemic AAV therapy. *Mol Ther* 2023;**31**:3123−6.
8. Wilson JM, Flotte TR. Moving forward after two deaths in a gene therapy trial of myotubular myopathy. *Hum Gene Ther* 2020;**31**: 695−6.
9. Lek A, Wong B, Keeler A, Blackwood M, Ma K, Huang S, et al. Death after high-dose rAAV9 gene therapy in a patient with Duchenne's muscular dystrophy. *N Engl J Med* 2023;**389**:1203−10.
10. Forrester JV, McMenamin PG, Dando SJ. CNS infection and immune privilege. *Nat Rev Neurosci* 2018;**19**:655−71.
11. Gao J, Gunasekar S, Xia ZJ, Shalin K, Jiang C, Chen H, et al. Gene therapy for CNS disorders: modalities, delivery and translational challenges. *Nat Rev Neurosci* 2024;**25**:553−72.
12. Peters CW, Maguire CA, Hanlon KS. Delivering AAV to the central nervous and sensory systems. *Trends Pharmacol Sci* 2021;**42**:461−74.
13. Keiser MS, Ranum PT, Yrigollen CM, Carrell EM, Smith GR, Muehlmatt AL, et al. Toxicity after AAV delivery of RNAi expression constructs into nonhuman primate brain. *Nat Med* 2021;**27**:1982−9.
14. Ortinski PI, Dong J, Mungenast A, Yue C, Takano H, Watson DJ, et al. Selective induction of astrocytic gliosis generates deficits in neuronal inhibition. *Nat Neurosci* 2010;**13**:584−91.
15. Suriano CM, Kumar N, Verpeut JL, Ma J, Jung C, Dunn CE, et al. An innate immune response to adeno-associated virus genomes decreases cortical dendritic complexity and disrupts synaptic transmission. *Mol Ther* 2024;**32**:1721−38.
16. Guo YW, Chen JL, Ji WY, Xu L, Xie Y, He S, et al. High-titer AAV disrupts cerebrovascular integrity and induces lymphocyte infiltration in adult mouse brain. *Mol Ther, Methods Clin Dev* 2023;**31**:101102.
17. Muhuri M, Maeda Y, Ma H, Ram S, Fitzgerald KA, Phillip WL, et al. Overcoming innate immune barriers that impede AAV gene therapy vectors. *J Clin Investig* 2021;**131**:e143780.
18. Dhungel BP, Winburn I, Pereira CD, Huang K, Chhabra A, Rasko JEJ. Understanding AAV vector immunogenicity: from particle to patient. *Theranostics* 2024;**14**:1260−88.

19. Costa Verdera H, Kuranda K, Mingozzi F. AAV vector immunogenicity in humans: a long journey to successful gene transfer. *Mol Ther* 2020;**28**:723−46.
20. Xu Y, Bai X, Lin J, Lu K, Weng S, Wu Y, et al. Intracranial AAV administration dose-dependently recruits B cells to inhibit the AAV redosing. *Mol Ther, Methods Clin Dev* 2025;**33**:101420.
21. Chan YK, Wang SK, Chu CJ, Copland DA, Letizia AJ, Costa Verdera H, et al. Engineering adeno-associated viral vectors to evade innate immune and inflammatory responses. *Sci Transl Med* 2021;**13**: eabd3438.
22. Decout A, Katz JD, Venkatraman S, Ablasser A. The cGAS−STING pathway as a therapeutic target in inflammatory diseases. *Nat Rev Immunol* 2021;**21**:548−69.
23. Chen C, Xu P. Cellular functions of cGAS−STING signaling. *Trends Cell Biol* 2023;**33**:630−48.
24. Chandler LC, Barnard AR, Caddy SL, Patricio MI, McClements ME, Fu H, et al. Enhancement of adeno-associated virus-mediated gene therapy using hydroxychloroquine in murine and human tissues. *Mol Ther, Methods Clin Dev* 2019;**14**:77−89.
25. Costa-Verdera H, Meneghini V, Fitzpatrick Z, Abou Alezz M, Fabyanic E, Huang X, et al. AAV vectors trigger DNA damage response-dependent pro-inflammatory signalling in human iPSC-derived CNS models and mouse brain. *Nat Commun* 2025;**16**:3694.
26. Hou YF, Wang ZM, Liu PY, Wei XB, Zhang ZY, Fan SL, et al. SMPDL3A is a cGAMP-degrading enzyme induced by LXR-mediated lipid metabolism to restrict cGAS−STING DNA sensing. *Immunity* 2023;**56**:2492−507.
27. Ye D, Chukwu C, Yang Y, Hu Z, Chen H. Adeno-associated virus vector delivery to the brain: technology advancements and clinical applications. *Adv Drug Deliv Rev* 2024;**211**:115363.
28. Christine CW, Richardson RM, Van Laar AD, Thompson ME, Fine EM, Khwaja OS, et al. Safety of AADC gene therapy for moderately advanced Parkinson disease three-year outcomes from the PD-1101 trial. *Neurology* 2022;**98**:E40−50.
29. Chen Q, Sun L, Chen ZJ. Regulation and function of the cGAS−STING pathway of cytosolic DNA sensing. *Nat Immunol* 2016;**17**:1142−9.
30. Dvorkin S, Cambier S, Volkman HE, Stetson DB. New frontiers in the cGAS−STING intracellular DNA-sensing pathway. *Immunity* 2024; **57**:718−30.
31. Zhou XG, Wang J, Yu L, Qiao G, Qin DL, Law BYK, et al. Mitophagy and cGAS−STING crosstalk in neuroinflammation. *Acta Pharm Sin B* 2024;**14**:3327−61.
32. Sun LJ, Wu JX, Du FH, Chen X, Chen ZJJ. Cyclic GMP−AMP synthase is a cytosolic DNA sensor that activates the type I interferon pathway. *Science* 2013;**339**:786−91.
33. Yang K, Tang Z, Xing C, Yan N. STING signaling in the brain: molecular threats, signaling activities, and therapeutic challenges. *Neuron* 2024;**112**:539−57.
34. Zhang XW, Bai XC, Chen ZJJ. Structures and mechanisms in the cGAS−STING innate immunity pathway. *Immunity* 2020;**53**:43−53.
35. Fisher TM, Liddelow SA. Emerging roles of astrocytes as immune effectors in the central nervous system. *Trends Immunol* 2024;**45**: 824−36.
36. Zengeler KE, Lukens JR. Innate immunity at the crossroads of healthy brain maturation and neurodevelopmental disorders. *Nat Rev Immunol* 2021;**21**:454−68.
37. Lu XY, Wang SA, Hua X, Chen X, Zhan MT, Hu QY, et al. Targeting the cGAS−STING pathway inhibits peripheral T-cell lymphoma progression and enhances the chemotherapeutic efficacy. *Adv Sci* 2024;**11**:e2306092.
38. Wang X, Zhang H, Wang Y, Bramasole L, Guo K, Mourtada F, et al. DNA sensing *via* the cGAS/STING pathway activates the immunoproteasome and adaptive T-cell immunity. *EMBO J* 2023;**42**: e110597.
39. Lin R, Zhou Y, Yan T, Wang R, Li H, Wu Z, et al. Directed evolution of adeno-associated virus for efficient gene delivery to microglia. *Nat Methods* 2022;**19**:976−85.
40. Yang L, Li S, Hou C, Zhang Y, Cheng L, Wang Z, et al. Biomimetic nanoregulators mediated tyrosine hydroxylase mRNA and stimulator of interferon genes antagonist codelivery for synergistic therapy on Parkinson's disease. *ACS Nano* 2025;**19**:33734−48.
41. Luo N, Lin K, Cai Y, Sui X, Zhang Z, Xing J, et al. Microglia-specific transduction *via* AAV11 armed with IBA1 promoter and miRNA-9 targeting sequences. *bioRxiv* 2024.
42. Wu J, Wang Y, Li X, Ouyang P, Cai Y, He Y, et al. Microglia replacement halts the progression of microgliopathy in mice and humans. *Science* 2025;**389**:eadr1015.
43. Haag SM, Gulen MF, Reymond L, Gibelin A, Abrami L, Decout A, et al. Targeting STING with covalent small-molecule inhibitors. *Nature* 2018;**559**:269−73.
44. Gulen MF, Samson N, Keller A, Schwabenland M, Liu C, Glück S, et al. cGAS−STING drives ageing-related inflammation and neurodegeneration. *Nature* 2023;**620**:374−80.
45. Yu CH, Davidson S, Harapas CR, Hilton JB, Mlodzianoski MJ, Laohamonthonkul P, et al. TDP-43 triggers mitochondrial DNA release *via* mPTP to activate cGAS/STING in ALS. *Cell* 2020;**183**: 636−49.
46. Xie X, Ma G, Li X, Zhao J, Zhao Z, Zeng J. Activation of innate immune cGAS−STING pathway contributes to Alzheimer's pathogenesis in 5xFAD mice. *Nat Aging* 2023;**3**:202−12.
47. Xiong WJ, Wu DM, Xue YL, Wang SK, Chung MJ, Ji XK, et al. AAV-regulatory sequences are correlated with ocular toxicity. *Proc Natl Acad Sci USA* 2019;**116**:5785−94.
48. Wang D, Tai PWL, Gao GP. Adeno-associated virus vector as a platform for gene therapy delivery. *Nat Rev Drug Discov* 2019;**18**: 358−78.
49. Keeler AM, Zhan W, Ram S, Fitzgerald KA, Gao G. The curious case of AAV immunology. *Mol Ther* 2025;**33**:1946−65.
50. Guillou J, De Pellegars A, Porcheret F, Frémeaux-Bacchi V, Allain-Launay E, Debord C, et al. Fatal thrombotic microangiopathy case following adeno-associated viral gene therapy. *Blood Adv* 2022;**6**: 4266−70.
51. Li C, Samulski RJ. Engineering adeno-associated virus vectors for gene therapy. *Nat Rev Genet* 2020;**21**:255−72.
52. Greenhalgh AD, David S, Bennett FC. Immune cell regulation of glia during CNS injury and disease. *Nat Rev Neurosci* 2020;**21**:139−52.
53. Greenhalgh AD, David S, Bennett FC. Immune cell regulation of glia during CNS injury and disease. *Nat Rev Neurosci* 2020;**21**:139−52.
54. Wang SK, Lapan SW, Hong CM, Krause TB, Cepko CL. *In situ* detection of adeno-associated viral vector genomes with SABER-FISH. *Mol Ther, Methods Clin Dev* 2020;**19**:376−86.
55. Blest HTW, Redmond A, Avissar J, Barker J, Bridgeman A, Fowler G, et al. HSV-1 employs UL56 to antagonize expression and function of cGAMP channels. *Cell Rep* 2024;**43**:114122.
56. Blest HTW, Chauveau L. cGAMP the travelling messenger. *Front Immunol* 2023;**14**:1150705.
57. Shinde O, Boyer JA, Cambier S, Vanportfliet JJ, Sui XW, Yadav GP, et al. Structures of ATP-binding cassette transporter ABCC1 reveal the molecular basis of cyclic dinucleotide cGAMP export. *Immunity* 2025; **58**:59−73.
58. Woo MS, Mayer C, Binkle-Ladisch L, Sonner JK, Rosenkranz SC, Shaposhnykov A, et al. STING orchestrates the neuronal inflammatory stress response in multiple sclerosis. *Cell* 2024;**187**:4043−60.
59. Xu YF, Wang Q, Wang J, Qian CY, Wang YS, Lu S, et al. The cGAS−STING pathway activates transcription factor TFEB to stimulate lysosome biogenesis and pathogen clearance. *Immunity* 2025;**58**: 309−25.
60. Liu BX, Carlson RJ, Pires IS, Gentili M, Feng EL, Hellier Q, et al. Human STING is a proton channel. *Science* 2023;**381**:508−14.
61. Zhang R, Yu C, Zeh HJ, Wang H, Kroemer G, Klionsky DJ, et al. Nuclear localization of STING1 competes with canonical signaling to activate AHR for commensal and intestinal homeostasis. *Immunity* 2023;**56**:2736−27354 e8.
62. Yuan B, Zhou XM, You ZQ, Xu WD, Fan JM, Chen SJ, et al. Inhibition of AIM2 inflammasome activation alleviates GSDMD-induced

pyroptosis in early brain injury after subarachnoid haemorrhage. *Cell Death Dis* 2020;**11**:76.
63. Rathinam VA, Vanaja SK, Fitzgerald KA. Regulation of inflammasome signaling. *Nat Immunol* 2012;**13**:333−42.
64. Cideciyan AV, Jacobson SG, Beltran WA, Sumaroka A, Swider M, Iwabe S, et al. Human retinal gene therapy for Leber congenital amaurosis shows advancing retinal degeneration despite enduring visual improvement. *Proc Natl Acad Sci U S A* 2013;**110**:E517−25.
65. Bozoglu T, Lee S, Ziegler T, Jurisch V, Maas S, Baehr A, et al. Endothelial retargeting of AAV9 *in vivo*. *Adv Sci (Weinh)* 2022;**9**:e2103867.
66. Xiong W, Wu DM, Xue Y, Wang SK, Chung MJ, Ji X, et al. AAV *cis*-regulatory sequences are correlated with ocular toxicity. *Proc Natl Acad Sci U S A* 2019;**116**:5785−94.
67. Chen S, Zhang Z, Zheng Z, Li A, Wei CX, Barnstable CJ, et al. Activation of Piezo 1 in the pathogenesis of glaucoma. *NPT* 2025;**2**: 13−25.
68. Martino AT, Suzuki M, Markusic DM, Zolotukhin I, Ryals RC, Moghimi B, et al. The genome of self-complementary adeno-associated viral vectors increases toll-like receptor 9-dependent innate immune responses in the liver. *Blood* 2011;**117**:6459−68.